

This is an Open Access document downloaded from ORCA, Cardiff University's institutional repository: <https://orca.cardiff.ac.uk/id/eprint/95118/>

This is the author's version of a work that was submitted to / accepted for publication.

Citation for final published version:

Khandu, ., Awange, Joseph L., Kuhn, M., Anyah, R. and Forootan, Ehsan 2017. Changes and variability of precipitation and temperature in the Ganges-Brahmaputra-Meghna River Basin based on global high-resolution reanalyses. *International Journal of Climatology* 37 (4) , pp. 2141-2159. 10.1002/joc.4842

Publishers page: <http://dx.doi.org/10.1002/joc.4842>

Please note:

Changes made as a result of publishing processes such as copy-editing, formatting and page numbers may not be reflected in this version. For the definitive version of this publication, please refer to the published source. You are advised to consult the publisher's version if you wish to cite this paper.

This version is being made available in accordance with publisher policies. See <http://orca.cf.ac.uk/policies.html> for usage policies. Copyright and moral rights for publications made available in ORCA are retained by the copyright holders.



# Changes and variability of precipitation and temperature in the Ganges-Brahmaputra-Meghna River Basin based on global high-resolution reanalyses

Khandu<sup>a</sup>, Joseph L. Awange<sup>a,b</sup>, Michael Kuhn<sup>a</sup>, Richard Anyah<sup>c</sup>, Eshan Forootan<sup>d,e</sup>

<sup>a</sup>*Western Australian Centre for Geodesy and the Institute for Geoscience Research, Curtin University, Western Australia, Australia*

<sup>b</sup>*Department of Cartographic Engineering, Universidade Federal de Pernambuco, Recife, Pernambuco, Brazil*

<sup>c</sup>*Associate Professor, Department of Natural Resources and the Environment, University of Connecticut, Storrs, Connecticut, USA*

<sup>d</sup>*Institute of Geodesy and Geoinformation, University of Bonn, Bonn, Germany*

<sup>e</sup>*School of Earth and Ocean Sciences, Cardiff University, Cardiff, UK*

---

## Abstract

1 Many previous studies have suggested that climate change impacts significantly  
2 on the hydro-climatic processes within the Ganges-Brahmaputra-Meghna (GBM)  
3 River Basin (RB). This study examines the observed climate characteristics  
4 and potential strengths and limitations of recent global high-resolution reanal-  
5 yses and satellite remote-sensing (SRS) products over the GBM RB for the  
6 most recent period (1980-2013) by (i) estimating trends and interannual vari-  
7 ations of precipitation and temperature and (ii) isolating precipitation varia-  
8 tions likely associated with El Niño Southern Oscillation (ENSO) and Indian  
9 Ocean Dipole (IOD). The surface temperature trends show widespread warming  
10 across the basin with a maximum increase of 0.6°C/decade over western Nepal  
11 and southern Tibet from 1980–2013. Rainfall changes over 1980–2013 indicated  
12 pronounced decline over high rainfall regions of northeast India, Bhutan, Nepal,  
13 and Bangladesh, especially from 1998–2013. Basin-averaged trends show rainfall  
14 declines of up to 39 mm/decade in June-August in the Brahmaputra-Meghna  
15 RB from 1998–2013. Temperature variability based on Principal Component  
16 Analysis (PCA) indicates that the first mode is associated with sea surface  
17 temperature (SST) warming in the Arabic Sea and the western tropical Pacific

18 Ocean, while the second mode appears to be significantly correlated to SST  
19 anomalies in the western (eastern) tropical Indian (Pacific) Ocean. The results  
20 also indicate that ENSO and IOD events significantly influence rainfall vari-  
21 ability, contributing to about 10–20% (ENSO) and 8–10% (IOD) to the annual  
22 rainfall, mainly over the Bhutan, Nepal, Bangladesh, and northeastern India.  
23 The quality of reanalysis products is highly variable over the GBM RB. MERRA  
24 (Modern-Era Retrospective Analysis for Research and Applications) agrees well  
25 with observed temperature data from the Climate Research Unit (CRU TS3.22),  
26 while ERA-Interim appears closer to observed precipitation datasets. Climate  
27 Forecast System Reanalysis (CFSR) shows the least seasonal and interannual  
28 skills among the three products.

*Keywords:* Ganges-Brahmaputra-Meghna River Basin, climate, reanalysis,  
satellite remote-sensing, precipitation, temperature

---

## 29 1. Introduction

30 Estimating long-term trends in surface air-temperature (hereinafter called  
31 “temperature”) and precipitation are crucial for identifying climate change. Pre-  
32 cipitation and temperature are two critical components of the water and energy  
33 cycles, and precipitation in particular, due to its high spatio-temporal variabil-  
34 ity, is one of the most difficult fluxes to simulate in dynamical models (*Flato*  
35 *et al.*, 2013). So, as critical as it is in the water and energy cycles, precipitation  
36 is a critical metric in the quality of many existing and emerging retrospective  
37 analyses (reanalyses). Evaluating climate models require consistent long-term  
38 observational records. Hydrological or land surface models, in particular, require  
39 high quality of climate forcing data (e.g., precipitation) to simulate other com-  
40 ponents of the water balance (e.g., soil moisture, (sub-) surface runoff) terms.  
41 Satellite remote-sensing (SRS)-based estimates and reanalyses offer an alter-  
42 native approach to *in-situ* observations where gauge-based networks are sparse  
43 and their analyses are often delayed or not shared across a common hydrological  
44 basin (*Duncan and Biggs*, 2012; *Peña-Arancibia et al.*, 2013).

45 Reanalysis outputs are generated by forecast models with fluxes constrained  
 46 by available gauge- and SRS-based observations, and thus are sensitive to both  
 47 the observing systems and model physics. The release of several global reanal-  
 48 yses over the past two decades (e.g., *Kalnay et al.*, 1996; *Onogi et al.*, 2005;  
 49 *Uppala et al.*, 2005; *Onogi et al.*, 2007; *Saha et al.*, 2010; *Dee et al.*, 2011; *Rie-*  
 50 *necker et al.*, 2011), provided several decades of various hydro-climatic data that  
 51 are highly valuable for understanding the global/regional climate change pro-  
 52 cess. The most widely used reanalysis products include those developed at the  
 53 National Centers for Environmental Prediction (NCEP)/National Center for At-  
 54 mospheric Research (NCAR) (see, *Kalnay et al.*, 1996; *Kanamitsu et al.*, 2002),  
 55 and at the European Center for Medium-Range Weather Forecasts (ECMWF)  
 56 (see, *Uppala et al.*, 2005; *Dee et al.*, 2011). Japan Meteorological Agency (JMA)  
 57 and the Central Research Institute of Electric Power Industry (CRIEPI) have  
 58 released two versions of reanalyses (JRA-25 and JRA-55) with the goal of pro-  
 59 viding consistent and high-quality reanalysis specifically over Asia (*Onogi et al.*,  
 60 2005, 2007; *Kobayashi et al.*, 2015). More recently, the National Aeronautic and  
 61 Space Administration (NASA) has produced a global high-resolution reanalysis  
 62 called the Modern-Era Retrospective Analysis for Research and Applications  
 63 (MERRA, *Rienecker et al.*, 2011) covering the satellite-era, while NCEP pro-  
 64 duced another high-resolution reanalysis called the Climate Forecast System  
 65 Reanalysis (CFSR, *Saha et al.*, 2010).

66 While reanalysis products are considered to be near-perfect representations  
 67 of the atmospheric state, they suffer from many deficiencies at various time-  
 68 and spatial-scales. Considering that many global high-resolution reanalyses  
 69 have become available during the past few years (e.g., *Saha et al.*, 2010; *Dee*  
 70 *et al.*, 2011; *Rienecker et al.*, 2011), it is vital to evaluate their skills in terms of  
 71 how they represent key climate features over different parts of the world. The  
 72 spatio-temporal heterogeneity of orography and climate (particularly, precipita-  
 73 tion) of the Ganges-Brahmaputra-Meghna (GBM) River Basin (RB) in South  
 74 Asia presents one of the most challenging tests to any observ<sup>ing</sup> and modelling  
 75 systems. The Indian summer monsoon, which dominates the annual rainfall

76 contribution (by 60–90%) is a result of complex interplay between the atmo-  
77 sphere, land, and the Indian ocean processes that takes place at various spatial-  
78 and temporal-scales. The pressure gradients that is formed between the south  
79 and north Indian ocean leads to a cross-equatorial flow in the lower troposphere,  
80 which carries enormous moisture towards the Indian sub-continent. These mon-  
81 soon rainfall pattern is further modulated by steep mountains of the Himalayas  
82 (*Barros et al., 2004*) along various stages of its flow in the GBM RB, resulting  
83 in numerous high rainfall spots and dry regions.

84 Only few studies have assessed the quality of rainfall and temperature vari-  
85 ability of reanalysis products over the GBM River Basin, with all of them fo-  
86 cussing over India and during the monsoon season (*Misra et al., 2012; Kishore*  
87 *et al., 2016*). *Kishore et al. (2016)* indicated that ECMWF reanalysis (ERA-  
88 Interim, *Dee et al., 2011*) was more closer to observed values than MERRA,  
89 CFSR, and JRA-25 during the monsoon season between 1989 and 2007. In an-  
90 other comparison study, *Misra et al. (2012)* indicated that there are significant  
91 differences in the climatology of evaporation in the three reanalyses: CFSR,  
92 MERRA, and NCEP II, which will have huge implications on precipitation and  
93 temperature across South Asia. Particularly, the study found significantly less  
94 continental evaporation in CFSR compared to MERRA and NCEP II, which  
95 may be attributed to how each reanalyses treat the atmospheric-land inter-  
96 actions. These results suggest that reanalysis products are still evolving and  
97 requires continuous validation over the Indian monsoon region.

98 This study examines the long-term trends and interannual variability of rain-  
99 fall and temperature over the GBM RB, using various existing gridded gauge-  
100 based datasets, and global high-resolution reanalyses over the period 1980–2013.  
101 The primary objective here is to assess the quality of three global high-resolution  
102 reanalyses: (i) ERA-Interim [ $0.79^\circ \times 0.79^\circ$ ], (ii) MERRA [ $0.50^\circ \times 0.67^\circ$ ], (iii)  
103 CFSR [ $0.50^\circ \times 0.50^\circ$ ], in estimating the long-term trends and the interannual  
104 variability of rainfall and temperature, which are important metrics for identi-  
105 fying climate change. The study is complemented by two SRS-based precipita-  
106 tion estimates: (i) Tropical Rainfall Measuring Mission (TRMM) Multisatellite

107 Precipitation Analysis (TMPA, 1998-2014) (*Huffman et al., 2007*) and (ii) Cli-  
 108 mate Hazards Group InfraRed Precipitation (CHIRP, 1982-2014) (*Funk et al.,*  
 109 *2012*), both of which have a relatively long period of precipitation records. Many  
 110 studies have already examined the seasonal skills of various existing SRS-based  
 111 precipitation estimates across different parts of the GBM RB (e.g., *Andermann*  
 112 *et al., 2011*; *Duncan and Biggs, 2012*; *Prakash et al., 2014*; *Khandu et al., 2016a*),  
 113 but have not addressed their long-term skills. Gauge-based datasets used here  
 114 include: Asian Precipitation Highly Resolved Observational Data Integration  
 115 Towards Evaluation of Water Resources (APHRODITE V1101, *Yatagai et al.,*  
 116 *2012*), Climate Research Unit (CRU TS3.22, *Harris et al., 2013*), and Global  
 117 Precipitation Climatology Centre (GPCC version 6, *Schneider et al., 2014*).

118 Section 2 describes the climatological characteristics of the GBM RB. In  
 119 Section 3, a brief review of the available rainfall and temperature datasets is  
 120 presented as well as the statistical methods used to analyse and compare the  
 121 various datasets. It also discusses the accuracy of several near-global high-  
 122 resolution SRS-based precipitation products in the region and their contribution  
 123 to the understanding of basin rainfall hydrology. The results are presented and  
 124 discussed in Section 4 and Section 5 concludes the study.

## 125 2. The Ganges-Brahmaputra-Meghna (GBM) River Basin (RB)

126 The GBM RB in South Asia is a combination of three large river basins  
 127 with a drainage area of about 1.7 million km<sup>2</sup> (*FAO, 2011*). Although the  
 128 three river basins have distinct physiological and climatological characteris-  
 129 tics even, it is considered to be one river basin that is shared by India (64%),  
 130 China (18%), Nepal (9%), Bangladesh (7%) and Bhutan (3%) (Fig. 1). The  
 131 three river systems join upstream of the GBM delta in Bangladesh to form the  
 132 third largest freshwater outlet (with a annual discharge of  $\sim 1,350$  km<sup>3</sup>) to the  
 133 world's oceans, being exceeded only by the Amazon and the Congo river sys-  
 134 tems (*Chowdhury and Ward, 2004*; *Steckler et al., 2010*). The headwaters of  
 135 Ganges (Brahmaputra) rivers originate from the Himalayan mountains of Gan-

136 gotori glaciers (northern slope of the Himalayas in Tibet) while the Meghna  
 137 river, originates in the mountains of north-eastern India. The Ganges is joined  
 138 by several smaller rivers (or tributaries) from across India and Nepal **form-**  
 139 **ing** one of the largest alluvial plains in northern India. A portion of Ganges  
 140 river (~50%) is diverted into the Hooghly river at Farakka Barrage before  
 141 reaching Bangladesh as a part of a treaty (called Farakka Treaty) signed be-  
 142 tween India and Bangladesh in 1996 to share the precious Ganges river (see,  
 143 [http://www.thewaterpage.com/farakka\\_water\\_treaty.htm](http://www.thewaterpage.com/farakka_water_treaty.htm)).

144 **[FIGURE 1 AROUND HERE.]**

145 The Brahmaputra river, also known as Yarlung Tsangpo (in Tibet), flows  
 146 eastwards before turning southwards into Arunachal Pradesh (India). It then  
 147 turns westwards, which is joined by many tributaries from northeast India and  
 148 Bhutan, **before entering** Bangladesh (also called Jamuna). The Meghna river  
 149 originates from the hilly mountains of Manipur (India), flowing southwest to  
 150 join the Ganges and Brahmaputra rivers that together flow into the Bay of  
 151 Bengal and a small part of West Bengal (India) forming the greatest deltaic  
 152 plain in the world at the confluence.

153 The GBM RB features distinct climatic characteristics due to the Indian  
 154 monsoon variability and unique topographic regime that includes the Himalayan  
 155 mountains and great plains of Ganges, Terai, parts of northeast India, and  
 156 Bangladesh. These irregular topographic variations significantly impact on the  
 157 spatial precipitation distribution through alteration of monsoonal flow, result-  
 158 ing in pronounced orographic rainfall along the Southern Foothills of Nepal,  
 159 Bhutan and northeast India and considerably lower rainfall on the lee sides of  
 160 the mountains and the western Ganges RB. The Ganges RB is characterized by  
 161 significant snowfall and precipitation in the northwest of its upper region and  
 162 very high precipitation in the areas downstream regions (such as the delta re-  
 163 gions of Bangladesh). The downstreams areas of Brahmaputra RB are directly  
 164 located on the monsoon flow and hence, some of the areas receive significantly  
 165 higher rainfall than the Ganges, while the world's highest precipitation is re-



166 ceived at Cherapunji (Meghalaya, India) located in the Meghna RB.

167 The winter precipitation over the western Himalayas is mainly driven by  
168 the mid-latitude sub-tropical jets known as the Western Disturbances, which is  
169 critical to the formation of snow/glaciers (*Dimri et al., 2015*). While the winter  
170 precipitation is well below 50 mm (as shown in Fig. 2a), the Indian monsoon  
171 accounts for 60-90% of the annual rainfall total in the GBM RB recording over  
172 1200 mm/month from June to September over Meghalaya (India) and southwest  
173 of Bhutan (Fig. 2b). The vector plots of winds (at 850 hPa pressure level) in  
174 Fig. 2 indicates the climate dynamics of the region e.g., winter (monsoon)  
175 precipitation is mainly forced by the westerlies of the Arabic Sea (southerlies  
176 of the Indian monsoon). The spatial temperature distribution is a function of  
177 altitude that decreases from as high as 40s ( $^{\circ}\text{C}$ ) during summer in the plains  
178 (e.g., Bangladesh) to as low as -30s ( $^{\circ}\text{C}$ ) in the Himalayas during winter. In  
179 this study, the Brahmaputra and Meghna RBs are treated as one river basin  
180 wherever a basin-average is calculated. The reason for merging them is that  
181 even though they have distinct climatological behaviours, they are affected by  
182 the monsoon at the same time.

183 [FIGURE 2 AROUND HERE.]

### 184 3. Data and methods

#### 185 3.1. Available observational data

186 Accurate and reliable estimation of precipitation requires dense gauge or  
187 radar networks **that** are not easily achievable in rugged Himalayan mountain  
188 regions (e.g., Bhutan and Nepal). Thus, gridded precipitation products based  
189 on *in-situ* observations may not accurately estimate rainfall where these gauge  
190 networks are sparse (e.g., *Duncan and Biggs, 2012; Khandu et al., 2016a*). Figure  
191 3 shows the spatial distribution of rain gauges over GBM RB that were used to  
192 derive (a) APHRODITE V1101 (hereinafter as APHRODITE), (b) CRU version  
193 TS3.22 (hereinafter as CRU.TS3.22), and (c) GPCC version 6 (hereinafter as  
194 GPCCv6). It is evident from Fig. 3 that gauge density is sparse across the GBM



195 RB, especially in the Tibetan region, western Ganges, Bhutan, Bangladesh, and  
196 northeast India. CRU\_TS3.22 has the least amount of stations (Fig. 3b).

197 **[FIGURE 3 AROUND HERE.]**

198 The accuracy of APHRODITE product was quantitatively evaluated across  
199 various parts of the GBM RB including Bhutan, Nepal, and India by various  
200 studies (e.g., *Rajeevan and Bhate, 2008*; *Andermann et al., 2011*; *Xue et al.,*  
201 *2013*; *Prakash et al., 2015*; *Khandu et al., 2016a*). *Andermann et al. (2011)*  
202 reported that APHRODITE shows the smallest error and high r-square values  
203 at both daily and monthly scales when compared to daily precipitation rates  
204 over Nepal. Comparison over India by *Rajeevan and Bhate (2008)* and *Prakash*  
205 *et al. (2015)* indicated that APHRODITE is well correlated ( $>0.6$ ) with high-  
206 quality Indian Meteorological Department (IMD) daily precipitation ( $1.0^\circ \times$   
207  $1.0^\circ$  grid) data. Over Bhutan, *Khandu et al. (2016a)* found that APHRODITE  
208 was comparable to independently gridded precipitation estimates. All of these  
209 studies demonstrate that APHRODITE is a reliable product at least for the  
210 validation period. *Prakash et al. (2015)* evaluated several land-based precipita-  
211 tion data including APHRODITE, CRU\_TS3.22, and GPCCv6 over India using  
212 high-density IMD rainfall data and indicated that APHRODITE and GPCCv6  
213 were highly correlated with IMD data. The study also reported that GPCCv6  
214 estimates were found to be quantitatively closer to IMD data during the mon-  
215 soon, while APHRODITE precipitation estimates are found to be lower than  
216 GPCCv6 and IMD datasets (see also, *Yatagai et al., 2012*).

217 Many global/near-global high-resolution SRS-based precipitation products  
218 have been released over the past decade with daily or finer temporal resolu-  
219 tions. Table 1 shows the details of various SRS-based precipitation products  
220 that have been applied across the GBM RB. The quality of these products  
221 have been investigated in a number of studies (e.g., *Yin et al., 2008*; *Ander-*  
222 *mann et al., 2011*; *Duncan and Biggs, 2012*; *Shrestha et al., 2012*; *Xue et al.,*  
223 *2013*; *Prakash et al., 2014*; *Khandu et al., 2016a*). These studies suggest that  
224 SRS-based estimates generally underestimate monsoon rainfall. Their limited

skills in detecting rainfall over rain-shadow regions and generally overestimating daily rainfall amounts over high-altitude regions is also reported in e.g., [Andermann et al. \(2011\)](#); [Duncan and Biggs \(2012\)](#); [Prakash et al. \(2014\)](#). Based on these findings, APHRODITE (1979–2007), GPCC (1979–2010) and TMPAv7 (1998–2013) precipitation estimates (both daily and monthly) are used to examine the long-term trends and variability of precipitation over the GBM RB and for evaluating various reanalysis products over the region. As a compromise between spatial resolution and estimation of long-term trends among different precipitation products, TMPAv7 product were linearly interpolated (using inverse distance weighting function) to a  $0.5^\circ \times 0.5^\circ$  grid resolution.

[TABLE 1 AROUND HERE.]

Currently, there exists several gridded temperature datasets derived from surface observations across the globe. A list of high-resolution gridded temperature datasets derived from *in-situ* observations are shown in Table 2. The daily mean ( $T_{\text{ave}}$ ) gridded temperature data made available by APHRODITE is the only high-resolution ( $0.25^\circ \times 0.25^\circ$ ) gauge-based product over Asia and covers the period from 1961–2007. A monthly time-series of gridded temperature data compiled from a recent version of the Global Historical Climatology Network (GHCN2) and several other sources has been released by the University of Delaware (UDEL, [Legates and Willmott, 1990](#); [Willmott and Robeson, 1995](#)). The dataset (currently version 3.01, UDELv3.01) has been recently used by [Chowdary et al. \(2014\)](#) to study the impacts of large-scale atmospheric-ocean interactions on surface temperature over India. CRU regularly updates its global-land surface temperature data (see, [Harris et al., 2013](#)) and is the mostly widely used temperature dataset globally.

[TABLE 2 AROUND HERE.]

### 3.2. Reanalysis products

Reanalyses have made significant contributions to the global/regional hydrological and climatic studies. With the release of many new high-resolution

reanalyses in the past decade (e.g., *Kalnay et al.*, 1996; *Onogi et al.*, 2007; *Saha et al.*, 2010; *Dee et al.*, 2011), their application into regional- and basin-scale studies have become increasingly valuable. Yet certain elements of the analyzed fields (e.g. precipitation) remain highly uncertain at global and regional scale both in terms of trends and interannual variabilities. The reliability of reanalysis fields can considerably vary in space and time due to lack of adequate observational data, instrumental changes, changing mix of observations, biases in observations, etc., which can introduce spurious variability and trends into reanalysis fields. Since reanalysis products are increasingly used as regional climate forcing data and hydrological model inputs, it is vital to estimate their accuracies. A reanalysis system consists of (i) a “data assimilation system” that combines available observations from various data sources and (ii) a “forecast model” consisting of an atmospheric model at its core, which is often coupled to a land surface model and/or ocean model (e.g., *Kalnay et al.*, 1996; *Dee et al.*, 2011; *Onogi et al.*, 2007).

Many reanalysis products have been assessed using gauge-based observations over various parts of the GBM RB (e.g., *Peña-Arancibia et al.*, 2013; *Shah and Mishra*, 2014; *Forsythe et al.*, 2014; *Kishore et al.*, 2016). *Shah and Mishra* (2014) evaluated MERRA, ERA-Interim, and CFSR with observed data from IMD, APHRODITE and TMPAv7 and found a precipitation (temperature) bias of 10% (-0.39°C), 34% (-0.21°C), and 11% (-0.44°C), respectively, during the monsoon over the Indian subcontinent. These products also failed to reproduce the observed trends in the monsoon season precipitation and temperature over India. *Kishore et al.* (2016) reported that precipitation fields of ERA-Interim, MERRA, CFSR, and JRA-25 generally showed very good correlation with IMD data and captured the annual cycle reasonably well. However, these studies are carried out at continental scales and there is a urgent need to address their potential applications in hydro-climatic studies over the GBM RB. Three global atmospheric reanalyses namely, (a) ERA-Interim/Land (*Balsamo et al.*, 2015), hereinafter referred to as ERA-Interim only, (b) MERRA Land (*Rienecker et al.*, 2011), hereinafter referred to as MERRA only, and (c) CFSR (*Saha et al.*,

285 2010) were considered here mainly because of their improvement in simulating  
 286 the land-surface state (see, Table 3 for details). These land-based reanalyses  
 287 has been particularly designed to accurately simulate the land-surface state  
 288 (moisture content/temperature) of soil, vegetation, and snow/ice to understand  
 289 the impacts of climate change in recent years (Rienecker *et al.*, 2011; Balsamo  
 290 *et al.*, 2015)

291 [TABLE 3 AROUND HERE.]

### 292 3.3. Sea surface temperature data

293 In order to determine the mechanisms for seasonal and interannual vari-  
 294 abilities of rainfall and temperature, their time-series were correlated with the  
 295 observed sea surface temperatures (SSTs) provided by the Met Office Hadley  
 296 Centre, UK. The Hadley Centre Global Sea Ice and Sea Surface Temperature  
 297 (HadISST, Rayner *et al.*, 2003) is a combination of monthly globally fields of  
 298 SST and sea ice concentration covering the period 1871-present. The global-  
 299 complete monthly HadISST data, which is provided at a  $1^\circ \times 1^\circ$  grid, is developed  
 300 using a complex process involving a reduced space optimal interpolation tech-  
 301 nique that is applied to SST data from the Marine Data Bank (mainly obtained  
 302 through ship tracks) and International Comprehensive Ocean-Atmospheric Data  
 303 Set (ICOADS) through to 1981. From here, these datasets are complemented  
 304 by a blend of *in-situ* and adjusted SRS-derived SSTs. Where the SSTs are  
 305 covered with ice, a different analysis is performed by combining sea ice data  
 306 from historical charts from shipping, expeditions and other activities, passive  
 307 microwave SRS retrievals, and NCEP operational ice analyses. Here, we use  
 308 HadISST data from 1980–2013 covering  $50^\circ\text{N}$ – $50^\circ\text{S}$ .

309 In addition, two ocean-atmospheric indices were used covering the same  
 310 period, namely: (a) Niño3.4 index (Trenberth, 1990) and (b) Dipole Mode Index  
 311 (DMI, Saji *et al.*, 1999) to examine the impacts of natural climate variabilities  
 312 such as El Niño Southern Oscillation (ENSO) and Indian Ocean Dipole (IOD),  
 313 respectively. It should be noted that ENSO and IOD variability may also be

314 influenced by long-term changes due to e.g., climate change. ENSO is commonly  
 315 measured by sea surface temperature (SST) anomalies in the equatorial Pacific  
 316 ocean, typically over (5°N–5°S, 120°–170°W), which is also known as Niño3.4  
 317 region (see, [Trenberth, 1990](#)). ENSO events are said to occur if SST anomalies  
 318 exceed 4°C for 6 months or more. Warm and cold ENSO phases are referred to as  
 319 El Niño and La Niña events, respectively, which are represented by anomalous  
 320 warming of the central and eastern tropical Pacific (warm phase), and vice  
 321 versa. ENSO events are marked by significant variations in surface and upper-  
 322 air conditions such as prolonged droughts and heavy rainfall events at the surface  
 323 and anomalous warming or cooling of the **upper-tropospheric lower-stratospheric**  
 324 (UTLS) region. Niño3.4 index was obtained from the National Oceanic and  
 325 Atmospheric Administration (NOAA, see, [http://www.esrl.noaa.gov/psd/  
 326 data/climateindices/list/](http://www.esrl.noaa.gov/psd/data/climateindices/list/)).

327 IOD is measured by the difference of SST anomalies between the western  
 328 (50°E–70°E and 10°S–10°N) and eastern (90°E–110°E and 10°S–0°S) equato-  
 329 rial Indian ocean, which is also referred to as **DMI**. Positive IOD events are  
 330 identified by a cooler than normal water in the tropical eastern Indian Ocean  
 331 and warmer than normal water in the tropical western Indian Ocean. **These pos-**  
 332 **itive IOD events** are associated with a shift of active convection from eastern  
 333 Indian Ocean to the west leading to potentially higher than normal rainfall over  
 334 parts of the Indian subcontinent. DMI **was** obtained from the Japan Agency  
 335 for Marine-Earth Science and Technology (see, [http://www.jamstec.go.jp/  
 336 frsgc/research/d1/iod/](http://www.jamstec.go.jp/frsgc/research/d1/iod/)).

### 337 3.4. Statistical analyses

338 Monthly rainfall and temperature anomalies **are** calculated relative to the  
 339 data period from e.g., 1980–2010 and long-term trends are **estimated and** tested  
 340 using both *parametric* (e.g., [Helsel and Hirsch, 2002](#), pp 221–264) and *non-*  
 341 *parametric* (e.g. [Mann, 1945](#); [Kendall, 1962](#); [Sen, 1968](#); [Hirsch and Slack, 1984](#))  
 342 methods. Parametric tests are considered to be more powerful but require data  
 343 to be independent and normally distributed, which is rarely the case for climate

344 datasets. Non-parametric methods on the other hand, do not require the as-  
345 sumption of normality and therefore, are considered to be more robust. Thus,  
346 both parametric and non-parametric tests are applied here to robustly deter-  
347 mine the trend estimates of precipitation and temperature. The two statistical  
348 methods are described in Appendix A1 and Appendix A2.

349 Further, both weather and climate are a result of complex non-linear inter-  
350 action between various components of the Earth system and contain significant  
351 temporal and spatial correlations, which makes the physical interpretation dif-  
352 ficult. Principal Component Analysis (PCA, Preisendorfer, 1988) is one of the  
353 widely used data exploratory tools used in atmospheric/oceanic science that  
354 allows for a space-time display of spatio-temporal data such as precipitation  
355 and temperature, in a very few modes. PCA is multipurpose and have been  
356 used in various geophysical and climatic applications for dimensionality reduc-  
357 tion (or removing irrelevant small-scale signals/noise), pattern extraction, and  
358 comparison of different datasets (see, Hannachi et al., 2007; Forootan, 2014,  
359 for a detailed review of its mathematical derivation and applications). PCA is  
360 applied here to isolate the likely influences of ENSO and IOD on the surface  
361 temperature changes in the GBM RB. A mathematical representation of the  
362 PCA method is briefly described in Appendix A3.

## 363 4. Results

### 364 4.1. Trend and amplitudes of rainfall and temperature

365 The mean annual amplitudes of monthly rainfall from gauge-based GPCCv6,  
366 SRS-based TMPAv7 and CHIRP, and three reanalysis products (i.e., ERA-  
367 Interim, MERRA, and CFSR) are shown in Fig. 4. Precipitation over the GBM  
368 RB shows significant spatial variability across all months as a result of the Indian  
369 monsoon and the orographic effects of the Himalayan mountains. The largest  
370 precipitation amplitudes are seen over the Brahmaputra-Meghna RB, while the  
371 Ganges RB show relatively low rainfall amplitudes except over few regions such  
372 as central Nepal (Fig. 4a–c). These annual amplitude maps closely relate the

average monsoon rainfall from June-September (JJAS) as indicated in Fig. 5. Note that the spatial patterns of JJAS rainfall is more localised, especially in the GPCCv7 data (Fig. 5a) indicating that SRS-based products depict a larger footprint (Fig. 5b-c). There are three regions: (a) Meghalaya, (b) southwest Bhutan, and (c) northern Arunuchal Pradesh that receive the highest monthly rainfall amount ( $\sim 1200$  mm during the JJAS) and hence shows the largest amplitude in all the observed datasets (Fig. 4a-c). Both TMPAv7 and CHIRP (1998–2013) show similar magnitudes of annual maps as GPCCv6 (Fig. 4b-c) but substantially underestimate monsoon rainfall in the high rainfall regions (Fig. 5b-c), albeit for different periods.

[FIGURE 4 AROUND HERE.]

[FIGURE 5 AROUND HERE.]

However, reanalysis products (specifically ERA-Interim and MERRA) significantly underestimate the annual amplitude (Fig. 4d-e) and the JJAS rainfall amount (Fig. 5d-e). MERRA, in particular failed to generate rainfall structures over Nepal and along the coastal areas of the Bay of Bengal (Fig. 4e and 5e), while both ERA-Interim and MERRA can barely represent the monsoon rainfall (Fig. 5d-e). CFSR, on the other hand, highly overestimates the annual amplitude and also misplaces the high rainfall region of southwest of Bhutan towards the east (Fig. 4f and 5f). While a strong agreement between TMPAv7 and GPCCv6 is expected, the differences between GPCCv6 and reanalysis products (especially, ERA-Interim and MERRA) is striking, given that both products are adjusted with observed rainfall datasets. For example, MERRA underestimates annual amplitude by 21–37% over the GBM RB (Table 4). CHIRP and APHRODITE estimates are also considerably lower than the other observed products over the basin (Table 4), which has been noted by *Prakash et al.* (2015).

[TABLE 4 AROUND HERE.]



Figure 6 shows the spatial variability of surface temperature over the GBM RB (over the period 1980–2010) based on observed data (CRU\_TS3.22 and UDEL) and three reanalysis products (ERA-Interim, MERRA, and CFSR). The annual amplitude of temperature increases with altitude with both CRU\_TS3.22 and UDEL gauge datasets (Fig. 6a–b) showing considerably high ( $>8^{\circ}\text{C}$ ) variations in the Tibetan region (located entirely in the Brahmaputra RB) and parts of the western Ganges RB (Indian region). The temperature varies between  $5^{\circ}\text{C}$  and  $8^{\circ}\text{C}$  in western Nepal, northern Bhutan, and Arunachal Pradesh (in India) while the lowest annual variations ( $\sim 5^{\circ}\text{C}$ ) are seen in Bangladesh and eastern India. The annual amplitude of temperature shown by the reanalysis products shows very similar spatial structures but their magnitudes varies considerably across the basin. While ERA-Interim tend to underestimate annual amplitudes (Fig. 6c), MERRA and CFSR products (Fig. 6d–e) overestimate annual amplitudes (by around  $3\text{--}4^{\circ}\text{C}$ ) with respect to CRU\_TS3.22 dataset, especially in the Ganges RB and in the Tibetan region. The basin averaged annual amplitudes (of temperature) are provided in Table 4, which indicates that MERRA depicts the largest annual variation followed by CFSR in the GBM RB. The maximum surface temperature over Ganges and Brahmaputra-Meghna basins occur during May and July, respectively, while their minimum temperatures occur in January.

[FIGURE 6 AROUND HERE.]

Changes in temperature and precipitation are estimated both in observations and reanalysis products for the period 1980–2010 using both parametric and non-parametric methods described in Section 3.4. However, precipitation trends are also calculated for the various time periods between 1980 and 2013 to shows the precipitation changes based on APHRODITE (1980–2007) and SRS-based (TMPAv7 and CHIRP) precipitation products. Rainfall trends between 1980 and 2007 are found to be negative (up to  $10\text{--}15\text{ mm/decade}$ ) mainly over the Ganges RB, consistently shown by all the observed products (i.e., APHRODITE, CRU\_TS3.22, GPCCv6, results not shown). Figure 7 shows the

precipitation changes over the GBM RB based on GPCCv6 (1980–2010), TMPAv7 and CHIRP (1998–2013), and the three reanalyses (1980–2010). While the changes in GPCCv6 are similar to those between 1980 and 2010 (Fig. 7a), significant increasing (decreasing) trends are seen from 1998–2013 over the western Ganges (Brahmaputra-Meghna) RBs showing large decreases (of about 20–30 mm/decade) over Bangladesh, northeast India, western Nepal, and southwestern Bhutan (Fig. 7b–c). Between 1998 and 2013, both TMPAv7 and CHIRP indicate strong decline of rainfall over the years in the Brahmaputra-Meghna RB (39 mm/dec in TMPAv6 during June–August). However, the increasing trend (12 mm/decade by TMPAv7) found over the Ganges RB is not replicated in CHIRP (Table 5) as it shows few areas with increasing trends in the western Ganges RB (Fig. 7c).

#### [FIGURE 7 AROUND HERE.]

Among the reanalyses, ERA-Interim tends to capture the observed trends but their magnitudes are significantly larger over western Nepal and eastern India (Fig. 7d) compared to GPCCv6 (Fig. 7a), while MERRA and CFSR show completely opposite signs of change over the Brahmaputra-Meghna RB (Fig. 7e–f). The magnitude of seasonal rainfall changes given in Table 5 shows decreasing rainfall in all the seasons over both the river basins especially in winter by most of the datasets including reanalysis products. Consistent with the spatial patterns (Fig. 7), MERRA and CFSR show anomalously large increasing trends during summer in the Brahmaputra-Meghna RB from 1980–2010 (Table 5). Precipitation changes in reanalyses depend on model parameterizations (e.g., convection scheme, moisture transport) and quality of assimilated observations and is also one of the most difficult physical processes to model. Instrumental changes and changing mix of observations might affect the precipitation fields by introducing spurious jumps. Another important factor to be considered is the models ability to simulate the weakening Indian monsoon circulation (*Ramanathan et al., 2005; Chung and Ramanathan, 2006*) and the affects of ENSO and IOD on the rainfall trends. The reliability of reanalyses to

461 some extent, are seasonally dependent as shown in Table 5.

462 [TABLE 5 AROUND HERE.]

463 Observed changes in temperature based on CRU\_TS3.22 and UDEL (Fig.  
464 8a–b) show significant warming over majority of the GBM basin with intense  
465 warming (up to 0.6°C/decade) over northern Brahmaputra RB (southern Ti-  
466 bet). The warming patterns are very similar between CRU\_TS3.22 and UDEL  
467 but the later did not show any significant warming over Bangladesh. The warm-  
468 ing trends in the northern parts of GBM RB are well captured by the reanalysis  
469 products, even though their magnitudes differ considerably over the region (Fig.  
470 8c–e). In reanalyses, temperature is still closely related to the model parame-  
471 terizations and model uncertainty may play some role in the representation of  
472 climate variability in reanalyses. Representation of temperature in reanalyses  
473 generally appears more robust than precipitation, likely due to direct assim-  
474 ilation of near surface temperature data from both radiosonde and satellite  
475 sources. However, ERA-Interim barely shows any significant warming over the  
476 region (Fig. 8c) despite their use of both near surface atmospheric temperature  
477 and water vapour to constrain soil moisture (Dee et al., 2011).

478 MERRA and CFSR (Fig. 8d–e) indicate few areas of negative spurious  
479 trends in the northern Brahmaputra (western Ganges) RB. CFSR also uses pre-  
480 cipitation observations over land to better constrain their soil moisture (Saha  
481 et al., 2010). The excessive warming seen in CFSR over the Himalayan re-  
482 gion (Fig. 8e) correlates well with the precipitation increases indicating that  
483 warming in this region may be caused by other changes such as limited water  
484 storage capacity in the coupled land model. The basin-averaged trends are es-  
485 timated for all the four seasons and are given in Table 6. Consistent with the  
486 spatial patterns observed in Fig. 8, the basin-averaged seasonal trends based  
487 on CRU\_TS3.22 and UDEL also indicates significant warming in both the river  
488 basins during the spring, autumn, and winter. CRU\_TS3.22 also showed signifi-  
489 cant warming trends (0.21°C/dec) in the Brahmaputra-Meghna RB during sum-  
490 mer. ERA-Interim was not able to reproduce these seasonal temperature trends,

491 but MERRA and CFSR agreed well with observed data in the Brahmaputra-  
492 Meghna RB (Table 6). Note that all the reanalysis products indicate negative  
493 (although not significant) temperature trends in summer over the Ganges RB.

494 [FIGURE 8 AROUND HERE.]

495 [TABLE 6 AROUND HERE.]

#### 496 4.2. Interannual variability of precipitation and temperature

497 The interannual variability of temperature and precipitation over the GBM  
498 basin was examined by applying PCA on the deseasonalized (annual and semi-  
499 annual components removed) and detrended (linear trend removed) anomalies of  
500 various products for the period 1980 to 2010. PCA was applied to the monthly  
501 anomalies (annual signals removed) of CRU\_TS3.22 to derive the EOFs (spatial  
502 patterns) and PCs (temporal patterns), while the rest of the datasets were pro-  
503 jected onto these EOFs to produce their temporal patterns. Only the first two  
504 leading modes are considered here due to their distinguished variance contribu-  
505 tion. Figure 9 shows the PCA modes of CRU\_TS3.22 temperature data together  
506 with the projected temporal components of UDEL and the three reanalysis tem-  
507 perature fields. The first orthogonal mode explains about 43% of the variance  
508 indicating strong positive anomalies over the western GBM RB and northern  
509 Brahmaputra basin (Fig. 9a). The second EOF (with a variance of 13%, Fig.  
510 9b) shows positive (negative) anomalies over Ganges (Brahmaputra-Meghna)  
511 RB and strong positive (negative) anomalies over central India (western Tibet).

512 [FIGURE 9 AROUND HERE.]

513 The first PC (Fig. 9c) shows considerable interannual variability, indicat-  
514 ing the extreme warm (e.g., 1988, 1999) and cold (e.g., 1997–1998, 2008–2009)  
515 episodes between 1998 and 2010. The patterns are quite similar in the second  
516 PC (Fig. 9d) but tend to differ during the periods 1982–1984 and 1996–2000.  
517 UDEL agrees very well with CRU\_TS3.22 with a correlation of 0.95 and 0.90  
518 for PC 1 and PC 2, respectively (Table 7). The temporal patterns are captured

519 very well by the reanalysis products (Fig. 9c-d), especially with ERA-Interim  
520 and MERRA showing high correlations with CRU\_TS3.22 (Table 7). The corre-  
521 lations between CRU\_TS.22 and MERRA for PC 2 is found to be higher (0.79)  
522 than those with ERA-Interim (0.68) whereas CFSR agrees only moderately for  
523 both the PCs.

524 [TABLE 7 AROUND HERE.]

525 In order to examine the mechanisms for these interannual variations, the  
526 two PCs (Fig. 9c-d) are correlated with the SST anomalies (50°N–50°S) for  
527 the period 1980 to 2010. It must be mentioned here that several studies have  
528 attempted to understand the role of SST variations on temperature, but were  
529 only focussed on the Indian sub-continent (*Hingane et al., 1985; Kothawale*  
530 *et al., 2010; Chowdary et al., 2014*). Figure 10 shows the correlation between  
531 the two PCs (Fig. 9c-d) and the SST anomalies (50°N–50°S). The two PCs are  
532 correlated with each grid element of the SST dataset to generate a temporal  
533 correlation as shown in Fig. 10. EOF 1 appears to be highly correlated with  
534 SST anomalies over the Arabian Sea, moderately correlated with SST anoma-  
535 lies over Bay of Bengal and the western tropical Pacific Ocean, and negatively  
536 correlated with SST over the western Pacific Ocean (Fig. 10a and c). This sug-  
537 gests that warm temperatures in the western Ganges basin are likely driven by  
538 local (i.e., Arabic Sea), and remote forcings such as weak La Niña-type events  
539 arising from warmer SSTs in the western tropical Pacific Ocean. EOF 2, on  
540 the other hand, is found to be highly correlated with SST anomalies in the  
541 western tropical Indian Ocean and the western tropical Pacific Ocean. The cor-  
542 relation patterns over the tropical Indian Ocean are similar to that of the IOD  
543 (*Saji et al., 1999*) and those over western tropical Pacific Ocean resemble the  
544 El Niño pattern indicating that both ENSO and IOD play a significant role in  
545 surface temperature variability across the GBM RB. Their effects are positive  
546 (negative) in the Ganges (Brahmaputra-Meghna) RB.

547 These correlation patterns are very weak in the reanalysis products with only  
548 MERRA (and to some extent ERA-Interim) being able to capture the spatial

patterns (Fig. 10e–h). Even though PC 1 of MERRA shows positive correlation over western tropical Pacific Ocean (Fig. 10e), their magnitudes are relatively closer to CRU\_TS3.22 than ERA-Interim (Fig. 10g–h) and CFSR (Fig. 10i–j). To quantify the relation between surface temperature and the remote SSTs, PC 2 (Fig. 9c) is correlated with Niño3.4 and DMI indices (Table 8). The correlation between PC 2 and Niño3.4 (DMI) is found to be 0.55 (0.23) based on observed CRU\_TS3.22 data and statistically significant at 5% significance level. Correlation with Niño3.4 index is higher for MERRA, followed by ERA-Interim and CFSR, which is found to be consistent with the spatial correlation patterns shown in Fig. 10. However, it is observed that CFSR temperature product is better correlated with DMI than those of MERRA and ERA-Interim. This results shown here are quite interesting because ERA-Interim, albeit having consistent temporal anomalies with respect to CRU\_TS3.22 indicates lower correlations with SSTs. This may lead to biases in seasonal precipitation amounts during major ENSO and IOD episodes.

[TABLE 8 AROUND HERE.]

To quantify the impact of ENSO and IOD on the rainfall variations over the GBM RB, the normalized ENSO/IOD indices (Niño3.4 and DMI) are fitted to the rainfall anomalies (annual signals removed) of APHRODITE (1998–2007), TMPAv7 (1998–2013), GPCCv6 (1980–2010), and the reanalysis products (1980–2010). The significance of the regression estimates are tested using a student’s *t*-test at 95% confidence level based on the correlations between Niño3.4/DMI indices and rainfall anomalies at each grid. Correlations between Niño3.4 (and DMI) and rainfall anomalies are found to be significant over few regions with values of up to 0.4 for Niño3.4 (and 0.3 for DMI). Figure 11 shows the rainfall contribution of ENSO and IOD on the total annual rainfall. In general, the positive ENSO mode (or El Niño) is associated with significant reduction of rainfall ( $\sim 15$  mm/yr) mainly over the western Ganges RB (including southern Nepal, Uttar Pradesh, Bihar, Meghalaya in India and southwest of Bhutan).

578 While the ENSO impacts are mainly concentrated over western Nepal and  
579 its surroundings from 1980 to 2007 (Fig. 11a), the period of 1998–2013 saw  
580 widespread reduction of rainfall in the Ganges and northern Brahmaputra RBs  
581 (Fig. 11b). However, a slight increase ( $\sim 5\text{--}10$  mm/yr) in rainfall can be seen  
582 over Bangladesh during the same period. The IOD mode (Fig. 11c–d), on the  
583 other hand is associated with increase (decrease) in rainfall in the southeastern  
584 parts of Ganges RB (Bangladesh and Meghalaya in India). During the same  
585 period, widespread decreases in rainfall are observed over Bangladesh, which  
586 are likely associated with frequent positive IOD events during the period (Fig.  
587 11d). Overall, the influence of ENSO is found to be more dominant ( $\sim 10\text{--}20\%$   
588 of total rainfall) than the IOD phenomenon ( $\sim 8\text{--}10\%$ ). These estimates were  
589 obtained by dividing the ENSO and IOD amplitudes by root-mean-squares of  
590 the total rainfall (see e.g., *Forootan et al., 2015*).

591 [FIGURE 11 AROUND HERE.]

592 The influence of ENSO and IOD on precipitation between 1980 and 2010  
593 shown by GPCCv6 (Fig. 12a and e) are found to be consistent with those  
594 indicated in APHRODITE from 1980–2007 (Fig. 11a and c), but with a slightly  
595 higher precipitation contribution in GPCCv6. This could be due to the more  
596 frequent events of La Niña (e.g., in 2007–2008) and El Niño (e.g., in 2006 and  
597 2009–2010) events towards the end of 2010 (see, *Khandu et al., 2016b*). Among  
598 the reanalysis products, ERA-Interim shows the closest agreement with gauge-  
599 based precipitation product, GPCCv6 (Fig. 12b and f) whereas MERRA (Fig.  
600 12c and g) and CFSR (Fig. 12d and h) either underestimate or overestimate  
601 rainfall contribution due to ENSO and IOD events. However, it should be  
602 noted that the spatial patterns of ENSO and IOD contributions are captured  
603 reasonably well by all the products.

604 [FIGURE 12 AROUND HERE.]



## 5. Conclusion

This study examined the seasonal and interannual variability of rainfall and temperature over the GBM RB using available observational gauge-, SRS-based, and global high-resolution reanalysis products covering the period 1980–2013. The reanalysis systems in particular, provide long time-series of climate datasets that are important for understanding various aspects of global/regional climate variability and change. They also act as reference climate forcing data for regional climate and hydrological modelling. The trend results indicate widespread warming across the GBM RB during the last 30 years. Warming appears to be more intense over the northern parts of the basin (western Nepal and Tibetan region) than the southern (e.g., Bangladesh) and western parts of the GBM RB with a maximum increase in temperature of  $0.6^{\circ}\text{C}/\text{decade}$  over the northern Brahmaputra RB (southern Tibet). Rainfall changes over various periods between 1980 and 2013 indicate significant decline over the GBM RB. In particular, SRS-based precipitation products such as TMPAv7 and CHIRP reveal pronounced monsoon rainfall decline over the last 15 years (from 1998–2013) in the high rainfall regions of northeast India, southwest Bhutan, Nepal, and Bangladesh ( $39\text{ mm}/\text{decade}$  during June–August). However, the monsoon rainfall appears to be increasing in the Ganges RB between 1998 and 2013 at a rate of  $12\text{ mm}/\text{decade}$ , but are found to be insignificant.

In terms of the interannual variations, temperature variations can be summarized in the first two orthogonal modes of PCA, which accounts for  $\sim 56\%$  of the total variability. The first EOF shows basin-wide positive anomalies with increasing magnitudes towards the west and north and are associated with warming SSTs over the Arabic Sea and the western tropical Pacific Ocean. The second EOF indicates a dipole-type pattern with positive (negative) anomalies over Ganges (Brahmaputra–Meghna) RBs and are significantly correlated to SST anomalies over western tropical Indian Ocean and eastern tropical Pacific Ocean. Thus, it is observed that surface temperature variations over the basin are both influenced by local (e.g., Arabic Sea) and remote (e.g., ENSO

and IOD) SST variations. Similarly, ENSO and IOD events are found to have significant influences on the seasonal rainfall across the GBM RB. The contribution of ENSO and IOD to the total annual rainfall is about 10–20% and 8–10%, respectively, affecting rainfalls mainly over southwest Bhutan, Nepal, northern Bangladesh, and northern parts of India (e.g., Bihar, Uttar Bangladesh, West Bengal, and Meghalaya).

The quality of the reanalysis products are found to be relatively poor over the GBM RB compared to the observed gauge-based datasets. It should be mentioned here that no single reanalysis is superior to others for both rainfall and temperature in reproducing the changes and variability. Among the reanalysis products examined in this study, MERRA temperature data is found to agree well with CRU\_TS3.22, while ERA-Interim is closer to GPCCv6 precipitation data in terms of trends and interannual variability. MERRA and ERA-Interim products are able to barely capture the spatial precipitation variability across the GBM RB during the monsoon, while CFSR tends to shift the high rainfall regions e.g., southwest of Bhutan, to the east. The annual amplitudes of MERRA precipitation fields is found to be significantly lower (by about 21–37%) compared to the GPCCv6 data, while CFSR overestimated it by about 9%. Despite showing considerable biases in precipitation and temperature, these products are able to represent the spatial patterns of ENSO and IOD contributions on precipitation.

## Acknowledgements

Khandu is grateful to Curtin Strategic International Research Scholarship, Curtin University (Australia) for the financial support. He also acknowledges the financial support of Prince Albert II of Monaco Foundation and the Intergovernmental Panel on Climate Change (IPCC). J. L. Awange acknowledges the financial support from Brazilian Science Without Borders Program/CAPES Grant No. 88881.068057/2014-01 in collaboration with the Federal University of Pernambuco (UFPE, Brazil). Further, the authors are grateful to APHRODITE,

Climate Research Unit (CRU), Global Precipitation Climatology Centre (GPCC), National Aeronautics and Space Administration (NASA), the Climate Prediction Center (CPC), and the European Centre for Medium-Range Weather Forecasts (ECMWF) for providing the necessary datasets used in this study.

## Appendix A1. Trend estimation

For illustration purposes, let us consider a matrix  $\mathbf{X}_{n \times m}$ , containing the time-series of monthly rainfall (or temperature) over the GBM RB, after removing their long-term temporal mean, where  $n$  describes the time (in months) and  $m$  represents the spatial locations (as stations or grids).

(i) **Multiple linear regression (MLR):** The MLR model can be formulated to characterize trends and seasonality in the dataset:

$$\mathbf{X} = x(j) = \beta_0 + \beta_1(j).t + \beta_2(j).\cos(2\pi t) + \beta_3(j).\sin(2\pi t) + \beta_4(j).\cos(4\pi t) + \beta_5(j).\sin(4\pi t) + \epsilon(t), \quad (1)$$

where  $\beta_0$ - $\beta_5$  are the coefficients of MLR for  $j = 1, \dots, m$ , and  $\epsilon$  are the residuals. The coefficients  $\beta_{1..5}(j)$  are estimated by the least squares adjustment method and represents the terms linear trends ( $\beta_1$ ), mean annual variability ( $\beta_2, \beta_3$ ), and semi-annual variability ( $\beta_4, \beta_5$ ). The inter-annual variability ( $\hat{\mathbf{X}}$ ) is usually related to large-scale ocean-atmospheric phenomenon such as ENSO and IOD modes, among others, and can be formulated as:

$$\hat{\mathbf{X}} = \hat{x}(j) - \left[ \hat{\beta}_1(j).t + \hat{\beta}_2(j).\cos(2\pi t) + \hat{\beta}_3(j).\sin(2\pi t) + \hat{\beta}_4(j).\cos(4\pi t) + \hat{\beta}_5(j).\sin(4\pi t) \right], \quad (2)$$

(ii) **Sen's slope estimation:** The least squares estimation of regression coefficient  $\hat{\beta}_1$  is vulnerable to gross errors and sensitive to non-normality of the probability distribution. [Sen \(1968\)](#)'s slope estimator is a common approach for assessing trends in hydrological time-series (e.g., precipitation)

as it is less sensitive to outliers. In this method, the slopes ( $T_i$ ) of all data pairs in time are first calculated by

$$T_i = \frac{x_k - x_l}{k - l} \quad \text{for } i = 1, 2, \dots, n, \quad (3)$$

where  $x_k$  and  $x_l$  are data values at time  $k$  and  $l$  ( $k > l$ ), respectively. The median values of these  $n$  values of  $T_i$  is the Sen's slope ( $\hat{\beta}$ ), which is calculated as:

$$\hat{\beta} = \begin{cases} T_{\frac{n+1}{2}} & n \text{ is odd} \\ \frac{1}{2} \left( T_{\frac{n}{2}} + T_{\frac{n+2}{2}} \right) & n \text{ is even} \end{cases} \quad (4)$$

where  $\beta$  can be both positive (increasing trend) or negative (decreasing trend).

## Appendix A2. Significance testing

The significance of linear trends estimated above should be tested by determining whether the derived trends in rainfall and temperature are significantly different from zero. Typically, the null hypothesis is  $H_0: \beta_1 = 0$  (no trend), while the alternative hypothesis,  $H_1: \beta_1 \neq 0$  (trend). Two approaches were used in this study and are briefly described below:

(i) **Mann-Kendall Test:** The Mann-Kendall test ([Mann, 1945](#); [Kendall, 1962](#)) is a non-parametric approach, which searches for a trend in time-series without specifying whether the trend is linear or non-linear. The test statistics ( $S$ ) is defined as:

$$S = \sum_{i=1}^{n-1} \sum_{j=i+1}^n \text{sgn}(x_j - x_i), \quad (1)$$

where  $n$  is the number of data points. Assuming  $(x_j - x_i) = \theta$ , the value of  $\text{sgn}(\theta)$  is calculated as:

$$\text{sgn}(\theta) = \begin{cases} 1 & \text{if } \theta > 0 \\ 0 & \text{if } \theta = 0 \\ -1 & \text{if } \theta < 0 \end{cases} \quad (2)$$

705 S represents the sum of positive and negative changes for all the data pairs  
 706 and for samples ( $n > 10$ ), the test is conducted using a normal distribution  
 707 with mean, variance, and test value of:

$$E[S] = 0$$

$$\text{Var}[S] = \frac{n(n-1)(2n+5) - \sum_{k=1}^n t_k(t_k-1)(2t_k+5)}{18}, \quad (3)$$

708

$$Z = \begin{cases} \frac{S-1}{\sqrt{\text{Var}(S)}} & \text{if } S > 0 \\ 0 & \text{if } S = 0 \\ \frac{S+1}{\sqrt{\text{Var}(S)}} & \text{if } S < 0 \end{cases} \quad (4)$$

709 If  $|Z| > z_{\alpha/2}$  (where  $\alpha/2$  indicates the quantile of the normal distribution),  
 710 the null hypothesis (no trend, denoted by  $H_0$ ) is rejected at  $\alpha$  significance  
 711 level (at 5%) in a two sided test. For seasonal and annual time-series,  
 712 it is also important to take into account the autocorrelation structure (or  
 713 serial correlation) in the data. Autocorrelation increases the probability of  
 714 detecting significant trends. [Hamed and Rao \(1998\)](#) suggested a modified  
 715 Mann-Kendall approach by considering the autocorrelation between the  
 716 ranks of the data. This is done by modifying the variance, Here, the  
 717 modified Mann-Kendall test was used and the null hypothesis was tested  
 718 at 95% confidence level.

719 (ii) **Student *t*-test**: Students *t*-test is one of the widely used method for  
 720 determining whether the trend is statistically significant. For example,  
 721 consider a time-series of rainfall anomalies ( $x(t)$ ) with an estimated linear  
 722 trend of  $\hat{\beta}_1$ , it's residuals ( $\epsilon(t)$ ) can be derived as difference of observed  
 723 rainfall anomalies ( $x(t)$ ) and those estimated from e.g., MLR model ( $\hat{x}(t)$ )  
 724 over  $t = 1, 2, \dots, n$  months:

$$\epsilon(t) = x(t) - \hat{x}(t), \quad (5)$$

725 and the standard error ( $S_\beta$ ) of  $\hat{\beta}_1$  is defined as

$$S_\beta = \frac{S_\epsilon}{\sqrt{\sum_{t=1}^n (t - \bar{t})^2}}, \quad (6)$$

726 where  $S_\epsilon^2$ , variance of the residuals ( $\epsilon$ ) is given by

$$S_\epsilon^2 = \frac{1}{n-2} \sum_{t=1}^n \epsilon(t)^2, \quad (7)$$

727 In order to examine whether the trend in  $x(t)$  is significantly different from  
 728 0, a test value is computed as a ratio between the estimated trend ( $\hat{\beta}_1$ )  
 729 and its standard error ( $S_\beta$ ):

$$t_\beta = \frac{\hat{\beta}_1}{S_\beta} \quad (8)$$

730 assuming that  $t_\beta$  follows a  $t$ -distribution. The null hypothesis (no trend  
 731 or  $H_0$  is rejected if  $|t| < t_{\text{crit}}$ , where  $t_{\text{crit}}$  is the point on the student's  
 732  $t$ -distribution with  $n - 2$  degrees of freedom. It should be noted that  
 733 while the  $t$ -test is simple and powerful to normally distributed data (e.g.,  
 734 temperature), it is less powerful against non-normally distributed data  
 735 (e.g., monthly rainfall).

### 736 **Appendix A3. Principal Component Analysis (PCA)**

737 The central idea of the PCA analysis is to find a set of orthogonal spatial pat-  
 738 terns (Empirical Orthogonal Functions or EOFs) along with a set of associated  
 739 uncorrelated time-series or principal components (PCs) that captures most of  
 740 the observed variance (expressed in %) from the available spatio-temporal data  
 741 such as precipitation and temperature. In summary, the EOF decomposition  
 742 can be written as  $\mathbf{X}_{(n,m)} \cong \mathbf{P}_{(n,k)} \mathbf{E}_{(m,k)}^T$  where  $\mathbf{X}_{(n,m)}$  is the time ( $n$ )-space  
 743 ( $m$ ) data (e.g., precipitation),  $\mathbf{E}_{(m,k)}$  contains the EOFs with  $k$  number of re-  
 744 tained modes, and  $\mathbf{P}_{(n,k)}$  are the PCs obtained by projecting the original data  
 745 ( $\mathbf{X}_{(n,m)}$ ) on the orthogonal base-functions  $\mathbf{E}_{(m,k)}$ , i.e.,  $\mathbf{P}_{(n,k)} = \mathbf{X}_{(n,m)} \mathbf{E}_{(m,k)}$ .  
 746 This method can be applied at various stages of the analysis in order to find  
 747 any meaningful links to various dynamics of the climate system using a subset  
 748 of PCs.

## 749 References

- 750 Andermann, C., S. Bonnet, and R. Gloaguen (2011), Evaluation of precipitation  
751 data sets along the Himalayan front, *Geochemistry, Geophysics, Geosystems*,  
752 7(12), doi:10.1029/2011GC003513.
- 753 Balsamo, G., C. Albergel, A. Beljaars, S. Boussetta, E. Brun, H. Cloke, D. Dee,  
754 E. Dutra, J. Muñoz-Sabater, F. Pappenberger, P. de Rosnay, T. Stockdale,  
755 and F. Vitart (2015), ERA-Interim/Land: A global land surface reanalysis  
756 data set, *Hydrol. Earth Syst. Sci.*, 19, 389–407, doi:10.5194/hess-19-389-2015.
- 757 Barros, A. P., G. Kim, E. Williams, and S. W. Nesbitt (2004), Probing oro-  
758 graphic controls in the Himalayas during the monsoon using satellite imagery,  
759 *Nat. Hazards Earth Syst. Sci.*, 4(1), 29–51, doi:10.5194/nhess-4-29-2004.
- 760 Chowdary, J. S., N. John, and C. Gnanaseelan (2014), Interannual variability  
761 of surface air-temperature over India: impact of ENSO and Indian Ocean sea  
762 surface temperature, *Int. J. Climatol.*, 34(2), 416–429, doi:10.1002/joc.3695.
- 763 Chowdhury, M. D. R., and N. Ward (2004), Hydro-meteorological variability in  
764 the greater Ganges-Brahmaputra-Meghna basins, *Int. J. Climatol.*, 24(12),  
765 1495–1508, doi:10.1002/joc.1076.
- 766 Chung, C. E., and V. Ramanathan (2006), Weakening of North Indian SST  
767 gradients and the monsoon rainfall in India and the Sahel, *J. Clim.*, 19,  
768 2036–2045, doi:10.1175/JCLI3820.1.
- 769 Dee, D. P., S. M. Uppala, A. J. Simmons, P. Berrisford, P. Poli, S. Kobayashi,  
770 U. Andrae, M. A. Balmaseda, , G. Balsamo, P. Bauer, P. Bechtold, A. C. M.  
771 Beljaars, L. van de Berg, J. Bidlot, N. Bormann, C. Delsol, R. Dragani,  
772 M. Fuentes, A. J. Geer, L. Haimbergere, S. B. Healy, H. Hersbach, E. V.  
773 Holm, L. Isaksen, P. Kållberg, M. Köhler, M. Matricardi, A. P. McNally,  
774 B. M. Monge-Sanz, J.-J. Morcrette, B.-K. Park, C. Peubey, P. de Rosnay,  
775 C. Tavalato, J.-N. Thépaut, and F. Vitarta (2011), The ERA-Interim reanal-



776 ysis: Configuration and performance of the data assimilation system, *Q. J.*  
777 *R. Meteorolog. Soc.*, 137, 553–597, doi:10.1002/qj.828.

778 Dimri, A. P., D. Niyogi, A. P. Barros, J. Ridley, U. C. Mohanty, T. Yasunari,  
779 and D. R. Sikka (2015), Western Disturbances: A Review, *Rev. Geophys.*,  
780 53(2), 225–246, doi:10.1002/2014RG000460.

781 Duncan, J. M., and E. M. Biggs (2012), Assessing the accuracy and applied  
782 use of satellite-derived precipitation estimates over Nepal, *Appl. Geogr.*, 34,  
783 626–638, doi:10.1016/j.apgeog.2012.04.001.

784 FAO (2011), Ganges-brahmaputra-meghna basin, *Tech. Rep. Water Report 37*,  
785 AQUASTAT, Food and Agriculture Organization of the United Nations,  
786 Rome, Italy, available from: [http://www.fao.org/nr/water/aquastat/  
787 basins/gbm/index.stm](http://www.fao.org/nr/water/aquastat/basins/gbm/index.stm). Accessed on 21 Feb 2015.

788 Flato, G., J. Marotzke, B. Abiodun, P. Braconnot, S. Chou, W. Collins, P. Cox,  
789 F. Driouech, S. Emori, V. Eyring, C. Forest, P. Gleckler, E. Guilyardi,  
790 C. Jakob, V. Kattsov, C. Reason, and M. Rummukainen (2013), Evaluation of  
791 climate, in *Climate Change 2013: The Physical Science Basis. Contribution*  
792 *of Working Group I to the Fifth Assessment Report of the Intergovernmental*  
793 *Panel on Climate Change*, edited by T. F. Stocker, D. Qin, G.-K. Plattner,  
794 M. Tignor, S. Allen, J. Boschung, A. Nauels, Y. Xia, V. Bex, and P. Midgley,  
795 Cambridge University Press, Cambridge, United Kingdom and New York,  
796 NY, USA.

797 Forootan, E. (2014), Statistical Signal Decomposition Techniques for Analyzing  
798 Time-Variable Satellite Gravimetry Data, Ph.D. thesis, Universität Bonn,  
799 Bonn, Germany.

800 Forootan, E., Khandu, J. L. Awange, M. Schumacher, R. Anyah, A. van Dijk,  
801 and J. Kusche (2015), Quantifying the impacts of ENSO and IOD on rain  
802 gauge and remotely sensed precipitation products over Australia, *Remote*  
803 *Sens. Environ.*, 172, 50–66, doi:10.1016/j.rse.2015.10.027.

804 Forsythe, N., S. Blenkinsop, and H. J. . Fowler (2014), Exploring objective  
805 climate classification for the Himalayan arc and adjacent regions using gridded  
806 data sources, *Earth Syst. Dynam.*, *6*, 311–326, doi:10.5194/esd-6-311-2015.

807 Funk, C., J. Michaelsen, and M. T. Marshall (2012), Mapping recent decadal  
808 climate variations in precipitation and temperature across eastern africa and  
809 the sahel, in *Remote Sensing of Drought: Innovative Monitoring Approaches*,  
810 edited by B. D. . Wardlow, M. C. . Anderson, and J. P. Verdin, chap. 14, pp.  
811 331–357, CRC Press 2012.

812 Funk, C. C., P. J. Peterson, M. F. Landsfeld, D. H. Pedreros, J. P. Verdin, J. D.  
813 Rowland, B. E. Romero, G. J. Husak, J. C. Michaelsen, and A. P. Verdin  
814 (2014), A quasi-global precipitation time series for drought monitoring, *U.S.*  
815 *Geol. Surv. Data Ser.*, *27*, 1062–1069, doi:10.1175/JCLI-D-13-00332.1.

816 Hamed, K. H., and A. R. Rao (1998), A modified Mann-Kendall trend  
817 test for autocorrelated data, *J. Hydrol.*, *204*(1-4), 182–196, doi:10.1016/  
818 S0022-1694(97)00125-X.

819 Hannachi, A., I. T. Jolliffe, and D. B. Stephenson (2007), Empirical orthogonal  
820 functions and related techniques in atmospheric science: A review, *Int. J.*  
821 *Climatol.*, *27*(9), 1119–1152, doi:10.1002/joc.1499.

822 Harris, I., P. Jones, T. Osborn, and D. Lister (2013), Updated high-resolution  
823 grids of monthly climatic observations- the CRU TS3.10 Dataset, *Int. J. Cli-*  
824 *matol.*, *34*(3), 623–642, doi:10.1002/joc.3711.

825 Helsel, D., and R. Hirsch (2002), Statistical methods in water resources, in  
826 *Techniques of Water Resources Investigations*, Book 4, chap. A3, p. 522pp,  
827 U.S. Geological Survey.

828 Hingane, L. S., K. R. Kumar, and B. V. R. Murty (1985), Long-term trends  
829 of surface air temperature in India, *Int. J. Climatol.*, *5*(5), 521–528, doi:  
830 10.1002/joc.3370050505.

831 Hirsch, R. M., and J. R. Slack (1984), A nonparametric trend test for seasonal  
832 data with serial dependence, *Water Resour. Res.*, 6(20), 727–732, doi:10.  
833 1029/WR020i006p00727.

834 Huffman, G. J., and D. T. Bolvin (2013), TRMM and other data precipita-  
835 tion data set documentation, *Tech. rep.*, Mesoscale Atmospheric Processes  
836 Laboratory, NASA Goddard Space Flight Center and Science Systems and  
837 Applications, Inc.

838 Huffman, G. J., D. T. Bolvin, E. J. Nelkin, D. B. Wolff, R. F. Adler, G. Gu,  
839 Y. Hong, K. P. Bowman, and E. F. Stocker (2007), The TRMM Multisatellite  
840 Precipitation Analysis (TMPA): Quasi-Global, Multiyear, Combined-Sensor  
841 Precipitation Estimates at Fine Scales, *J. Hydrometeorol.*, 8(1), 38–55, doi:  
842 10.1175/JHM560.1.

843 Joyce, R. J., J. E. Janowiak, P. A. Arkin, and P. Xie (2004), CMORPH: A  
844 method that produces global precipitation estimates from passive microwave  
845 and infrared data at high spatial and temporal resolution, *J. Hydrometeorol.*,  
846 5(3), 487–503, doi:10.1175/1525-7541(2004)005<0487:CAMTPG>2.0.CO;2.

847 Kalnay, E., M. Kanamitsu, R. Kistler, W. Collins, D. Deaven, L. Gandin,  
848 M. Iredell, S. Saha, G. White, J. Woollen, Y. Zhu, M. Chelliah, W. Ebisuzaki,  
849 W. Higgins, J. Janowiak, K. C. Mo, C. Ropelewski, J. Wang, A. Leet-  
850 maa, R. Reynolds, R. Jenne, , and D. Joseph (1996), The NCEP/NCAR  
851 40-year reanalysis project, *Bull. Am. Meteorol. Soc.*, 77(3), 437–470, doi:  
852 10.1175/1520-0477(1996)077<0437:TNYP>2.0.CO;2.

853 Kanamitsu, M., W. Ebisuzaki, J. Woollen, S.-K. Yang, J. J. Hnilo, M. Fiorino,  
854 and G. L. Potter (2002), NCEP-DOE AMIP-II Reanalysis (R-2), *Bull. Am.*  
855 *Meteorol. Soc.*, 83, 1631–1643, doi:10.1175/BAMS-83-11-1631.

856 Kendall, M. G. (1962), Rank correlation methods, *J. Am. Stat. Assoc.*, 63(324),  
857 1379–1389, doi:10.1080/01621459.1968.10480934.

858 Khandu, J. L. Awange, and E. Forootan (2016a), An evaluation of high-  
859 resolution gridded precipitation products over Bhutan (1998-2012), *Int. J.*  
860 *Climatol.*, *36*(3), 1067–1087, doi:10.1002/joc.4402.

861 Khandu, E. Forootan, M. Schumacher, J. Awange, and H. M. Schmied (2016b),  
862 Exploring the influence of precipitation extremes and human water use on to-  
863 tal water storage (twS) changes in Brahmaputra-Ganges-Meghna Basin, *Wa-*  
864 *ter Resour. Res.*, doi:10.1002/2015WR018113, accepted.

865 Kishore, P., S. Jyothi, G. Basha, S. V. B. Rao, M. Rajeevan, and I. Velicogna  
866 (2016), Precipitation climatology over India: validation with observations  
867 and reanalysis datasets and spatial trends, *Clim. Dyn.*, *46*(1), 541–556, doi:  
868 10.1007/s00382-015-2597-y.

869 Kobayashi, S., Y. Ota, Y. Harada, A. Ebata, M. Moriya, H. Onoda, K. Onogi,  
870 H. Kamahori, C. Kobayashi, H. Endo, K. Miyaoka, and K. Takahashi (2015),  
871 The JRA-55 Reanalysis: General specifications and basic characteristics,  
872 *Quart. J. R. Meteorol. Soc.*, *93*(1), 5–48, doi:10.2151/jmsj.2015-001.

873 Kothawale, D. R., , A. A. Munot, and K. K. Kumar (2010), Surface air temper-  
874 ature variability over India during 1901-2007, and its association with ENSO,  
875 *Clim. Res.*, *42*(1), 89–104, doi:10.3354/cr00857.

876 Legates, D. R., and C. J. Willmott (1990), Mean seasonal and spatial variability  
877 in global surface air temperature, *Theor. Appl. Climatol.*, *41*(1), 11–21, doi:  
878 10.1007/BF00866198.

879 Mann, H. B. (1945), Nonparametric tests against trend, *Econometrica*, *13*(3),  
880 245–259.

881 Misra, V., P. Pantina, S. C. Chan, and S. DiNapoli (2012), A comparative  
882 study of the Indian summer monsoon hydroclimate and its variations in three  
883 reanalyses, *Clim. Dyn.*, *39*(5), 1149–1168, doi:10.1007/s00382-012-1319-y.

884 Onogi, K., H. Koide, M. Sakamoto, S. Kobayashi, J. Tsutsui, H. Hatsushika,  
885 T. Matsumoto, N. Yamazaki, H. Kamahori, K. Takahashi, K. Kato, T. Ose,

886 S. Kadokura, and K. Wada (2005), JRA-2: Japanese 25-year Reanalysis,  
887 *Quart. J. R. Meteorol. Soc.*, *131*(613), 3259–3268, doi:10.1256/qj.05.88.

888 Onogi, K., J. Tsutsui, H. Koide, M. Sakamoto, S. Kobayashi, H. Hatsushika,  
889 T. Matsumoto, N. Yamazaki, H. Kamahori, K. Takahashi, S. Kadokura,  
890 K. Wada, K. Kato, R. Oyama, T. Ose, N. Mannoji, and R. Taira (2007),  
891 The JRA-25 Reanalysis, *Quart. J. R. Meteorol. Soc.*, *85*(3), 369–432, doi:  
892 10.2151/jmsj.85.369.

893 Peña-Arancibia, J. L., A. I. J. M. van Dijk, L. J. Renzullo, and M. Mulligan  
894 (2013), Evaluation of precipitation estimation accuracy in reanalyses, satellite  
895 products, and an ensemble method for regions in Australia and South and  
896 East Asia, *J. Hydrometeor.*, *4*(14), 1323–1333, doi:10.1175/JHM-D-12-0132.1.

897 Prakash, S., V. Sathiyamoorthy, C. Mahesh, and R. M. Gairola (2014), An eval-  
898 uation of high-resolution multisatellite rainfall products over the Indian mon-  
899 soon region, *Int. J. Remote Sens.*, *35*(9), 3018–3035, doi:10.1080/01431161.  
900 2014.894661.

901 Prakash, S., A. K. Mitra, I. M. Momin, E. N. Rajagopal, S. Basu, M. Collins,  
902 A. G. Turner, K. A. Rao, and K. Ashok (2015), Seasonal intercomparison  
903 of observational rainfall datasets over india during the southwest monsoon  
904 season, *Int. J. Remote Sens.*, *35*(9), 2326–2338, doi:10.1002/joc.4129.

905 Preisendorfer, R. W. (1988), *Principal component analysis in meteorology and*  
906 *oceanography*, 425 pp., Elsevier.

907 Rajeevan, M., and J. Bhate (2008), A high resolution daily gridded rainfall  
908 data set (1971-2005) for mesoscale meteorological studies, *Tech. Rep. NCC*  
909 *Research Report No. 9*, National Climate Centre, Indian Meteorological De-  
910 partment, Pune, India, available from [http://www.imdpune.gov.in/ncc\\_](http://www.imdpune.gov.in/ncc_rept/RESEARCH%20REPORT%209.pdf)  
911 [rept/RESEARCH%20REPORT%209.pdf](http://www.imdpune.gov.in/ncc_rept/RESEARCH%20REPORT%209.pdf), accessed on: 21 June 2014.

912 Rajeevan, M., and J. Bhate (2009), A high resolution daily gridded rainfall

dataset (1971-2005) for mesoscale meteorological studies, *Curr. Sci.*, *96*, 558–  
562.

Ramanathan, V., C. Chung, D. Kim, T. Bettge, L. Buja, J. T. Kiehl, W. M.  
Washington, Q. Fu, D. R. Sikka, , and M. Wild (2005), Atmospheric brown  
clouds: Impacts on South Asian climate and hydrological cycle, *Proc. Natl.  
Acad. Sci. U.S.A.*, *102*(15), 5326–5333, doi:10.1073pnas.0500656102.

Rayner, N. A., D. E. Parker, E. B. Horton, C. K. Folland, L. V. Alexander,  
D. P. Rowell, E. C. Kent, and A. Kaplan (2003), Global reanalyses of sea  
surface temperature, sea ice, and night marine air temperature since the late  
nineteenth century, *J. Geophys. Res.*, *108*(D14), doi:10.1029/2002JD002670.

Rienecker, M. M., M. J. Suarez, R. Gelaro, R. Todling, J. Bacmeister, E. Liu,  
M. G. Bosilovich, S. D. Schubert, L. Takacs, G. K. Kim, S. Bloom, J. Chen,  
D. Collins, A. Conaty, A. da Silva, W. Gu, J. Joiner, R. D. Koster, R. Lucch-  
esi, A. Molod, T. Owens, S. Pawson, P. Pegion, C. R. Redder, R. Reichle, F. R.  
Robertson, A. G. Ruddick, M. Sienkiewicz, and J. Woollen (2011), MERRA:  
NASA’s Modern-Era Retrospective Analysis for Research and Applications,  
*J. Clim.*, *24*(14), 3624–3648, doi:10.1175/JCLI-D-11-00015.1.

Saha, S., S. Moorthi, H.-L. Pan, X. Wu, J. Wang, S. Nadiga, P. Tripp, R. Kistler,  
J. Woollen, D. Behringer, H. Liu, D. Stokes, R. Grumbine, G. Gayno, J. Wang,  
Y. T. Hou, H. Y. Chuang, H.-M. H. Juang, J. Sela, M. Iredell, R. Treadon,  
D. Kleist, P. V. Delst, D. Keyser, J. Derber, M. Ek, J. Meng, H. Wei,  
R. Yang, S. Lord, H. V. D. Dool, A. Kumar, W. Wang, C. Long, M. Chelliah,  
Y. Xue, B. Huang, J.-K. Schemm, W. Ebisuzaki, R. Lin, P. Xie, M. Chen,  
S. Zhou, W. Higgins, C.-Z. Zou, Q. Liu, Y. Chen, Y. Han, L. Cucurull,  
R. W. Reynolds, G. Rutledge, and M. Goldberg (2010), The NCEP Climate  
Forecast System Reanalysis, *Bull. Am. Meteorol. Soc.*, *91*(8), 1015–1057, doi:  
10.1175/2010BAMS3001.1.

Saji, N. H., B. N. Goswami, P. N. Vinayachandran, and T. Yamagata (1999),  
A dipole mode in the tropical Indian Ocean, *Nature*, *401*, 360–363.

942 Schneider, U., A. Becker, P. Finger, A. M.-. Christoffer, M. Ziese, and B. Rudolf  
 943 (2014), GPCP's new land surface precipitation climatology based on quality-  
 944 controlled in situ data and its role in quantifying the global water cycle, *Theor.*  
 945 *Appl. Climatol.*, 115(1-2), 15–40, doi:10.1007/s00704-013-0860-x.

946 Sen, P. K. (1968), Estimates of the regression coefficient based on Kendall's  
 947 Tau, *J. Am. Stat. Assoc.*, 63(324), 1379–1389, doi:10.1080/01621459.1968.  
 948 10480934.

949 Shah, R., and V. Mishra (2014), Evaluation of the reanalysis products for the  
 950 monsoon season droughts in India, *J. Hydrometeor.*, 15(4), 1575–1591, doi:  
 951 10.1175/JHM-D-13-0103.1.

952 Shrestha, D., P. Singh, and K. Nakamura (2012), Spatiotemporal variation of  
 953 rainfall over the central Himalayan region revealed by TRMM Precipitation  
 954 Radar, *J. Geophys. Res.*, 117(D22), doi:10.1029/2012JD018140.

955 Sorooshian, S., K. Hsu, X. Gao, H. Gupta, B. Imam, and D. Braithwaitea  
 956 (2000), Evaluation of PERSIANN System Satellite-Based Estimates of trop-  
 957 ical rainfall, *Bull. Am. Meteorol. Soc.*, 81(9), 2035–2046.

958 Steckler, M. S., S. L. Nooner, S. H. Akhter, S. K. Chowdhury, S. Bettadpur,  
 959 L. Seeber, and M. G. Kogan (2010), Modeling Earth deformation from mon-  
 960 soonal flooding in Bangladesh using hydrographic, GPS, and Gravity Re-  
 961 covery and Climate Experiment (GRACE) data, *J. Geophys. Res.*, 15(B8),  
 962 doi:10.1029/2009JB007018.

963 Trenberth, K. E. (1990), Recent observed interdecadal climate changes in the  
 964 Northern Hemisphere, *Bull. Amer. Meteor. Soc.*, 71(7), 988993, doi:10.1175/  
 965 1520-0477(1990)071<0988:ROICCI>2.0.CO;2.

966 Turk, F. J., and S. D. Miller (2005), Toward improved characterization of  
 967 remotely sensed precipitation regimes with MODIS/AMSR-E blended data  
 968 techniques, *IEEE Trans. Geosci. Remote Sens.*, 43(5), 1059–1069, doi:  
 969 10.1109/TGRS.2004.841627.



970 Uppala, S. M., P. W. K  llberg, A. J. Simmons, U. Andrae, V. D. C. Bech-  
 971 told, M. Fiorino, J. K. Gibson, J. Haseler, A. Hernandez, G. A. Kelly,  
 972 X. Li, K. Onogi, S. Saarinen, N. Sokka, R. P. Allan, E. Andersson, K. Arpe,  
 973 M. A. Balmaseda, A. C. M. Beljaars, L. V. D. Berg, J. Bidlot, N. Bormann,  
 974 S. Caires, F. Chevallier, A. Dethof, M. Dragosavac, M. Fisher, M. Fuentes,  
 975 S. Hagemann, E. H  lm, B. J. Hoskins, L. Isaksen, P. A. E. M. Janssen,  
 976 R. Jenne, A. P. McNally, J.-F. Mahfouf, J.-J. Morcrette, N. A. Rayner, R. W.  
 977 Saunders, P. Simon, A. Sterl, K. E. Trenberth, A. Untch, D. Vasiljevic,  
 978 P. Viterbo, and J. Woollen (2005), The ERA-40 re-analysis, *Q. J. R. Me-*  
 979 *eteorolog. Soc.*, *131*, 2961–3012, doi:10.1256/qj.04.176.

980 Ushio, T., K. Sasashige, T. Kubota, S. Shige, K. Okamoto, K. Aonashi, T. In-  
 981 oue, N. Takahashi, and T. Iguchi (2009), A kalman filter approach to the  
 982 Global Satellite Mapping of Precipitation (GSMaP) from combined passive  
 983 microwave and infrared radiometric data, *J. Meteor. Soc. Japan*, *87A*(9),  
 984 3084–3097, doi:10.2151/jmsj.87A.137.

985 Willmott, C. J., and S. M. Robeson (1995), Climatologically aided interpolation  
 986 (CAI) of terrestrial air temperature, *Int. J. Climatol.*, *15*(2), 221–229, doi:  
 987 10.1002/joc.3370150207.

988 Xie, P., Y. Yarosh, T. Love, J. E. Janowiak, and P. A. Arkin (2002), A real-  
 989 time daily precipitation analysis over south asia, in *16th Conference of Hy-*  
 990 *drology*, NOAA/Climate Prediction Center, American Meteorological Society,  
 991 Orlando, Florida, available at: [http://www.cpc.ncep.noaa.gov/products/](http://www.cpc.ncep.noaa.gov/products/fews/sasia_rfe.pdf)  
 992 [fews/sasia\\_rfe.pdf](http://www.cpc.ncep.noaa.gov/products/fews/sasia_rfe.pdf).

993 Xie, P., M. Chen, S. Yang, A. Yatagai, T. Hayasaka, Y. Fukushima, and C. Liu  
 994 (2007), A gauge-based analysis of daily precipitation over East Asia, *J. Hy-*  
 995 *drometeorol.*, *8*(3), 607–626, doi:10.1175/JHM583.1.

996 Xue, X., Y. Hong, A. S. Limaye, J. J. Gourley, G. J. Huffman, S. I. Khan,  
 997 C. Dorji, and S. Chen (2013), Statistical and hydrological evaluation of  
 998 TRMM-based Multi-satellite Precipitation Analysis over the Wangchu Basin

999 of Bhutan: Are the latest satellite precipitation products 3b42v7 ready for  
1000 use in ungauged basins?, *J. Hydrol.*, *499*, 91–99, doi:10.1016/j.jhydrol.2013.  
1001 06.042.

1002 Yasutomi, N., A. Hamada, and A. Yatagai (2011), Development of a long-term  
1003 daily gridded temperature dataset and its application to rain/snow discrimi-  
1004 nation of daily precipitation, *Global Environ. Res.*, *V15N2*, 165–172.

1005 Yatagai, A., K. Kamiguchi, O. Arakawa, A. Hamada, N. Yasutomi, and A. Ki-  
1006 toh (2012), APHRODITE: Constructing a Long-term Daily Gridded Precipi-  
1007 tation Dataset for Asia based on a Dense Network of Rain Gauges, *Bull. Am.*  
1008 *Meteorol. Soc.*, *93*, 1401–1415, doi:10.1175/BAMS-D-11-00122.1.

1009 Yin, Z. Y., X. Zhang, X. Liu, M. Colella, and X. Chen (2008), An assessment  
1010 of the biases of satellite rainfall estimates over the Tibetan Plateau and cor-  
1011 rection methods based on topographic analysis, *J. Hydrometeor.*, *9*, 301–326,  
1012 doi:10.1175/2007JHM903.1.

Table 1: Details of rain gauge products and near-global high-resolution SRS-based precipitation products that have been regularly applied over various parts of the GBM RB.

Product	Period	Spatial Resl.	Temporal Resl.	Coverage	References
<b>Rain gauge products</b>					
APHRODITE	1951-2007	$0.25^\circ \times 0.25^\circ$	Daily	Asia	<a href="#">Yatagai et al. (2012)</a>
IMD	1971-2005	$1.0^\circ \times 1.0^\circ$	Daily	India	<a href="#">Rajeevan and Bhat (2009)</a>
GPCCv6	1901-2010	$0.50^\circ \times 0.50^\circ$	Monthly	Global-land	<a href="#">Schneider et al. (2014)</a>
CRU_TS3.23	1901-2014	$0.50^\circ \times 0.50^\circ$	Monthly	Global-land	<a href="#">Harris et al. (2013)</a>
CPC	1948-present	$0.25^\circ \times 0.25^\circ$	Daily	Global-land	<a href="#">Xie et al. (2007)</a>
<b>Satellite-based precipitation estimates</b>					
CHIRP	1981-present	$0.05^\circ \times 0.05^\circ$	Weekly	50S-50N	<a href="#">Funk et al. (2014)</a>
CMORPH	2003-present	$0.25^\circ \times 0.25^\circ$	3-hourly	50S-50N	<a href="#">Joyce et al. (2004)</a>
CPC-RFE	2001-present	$0.10^\circ \times 0.10^\circ$	Daily	South Asia	<a href="#">Xie et al. (2002)</a>
GSMaP_MVK	2002-present	$0.10^\circ \times 0.10^\circ$	1-hourly	60S-60N	<a href="#">Ushio et al. (2009)</a>
NRL-Blend	2002-present	$0.10^\circ \times 0.10^\circ$	3-hourly	60S-60N	<a href="#">Turk and Miller (2005)</a>
PERSIANN	2000-present	$0.25^\circ \times 0.25^\circ$	6-hourly	50S-50N	<a href="#">Sorooshian et al. (2000)</a>
TRMM 3B42v6	1998-2010	$0.25^\circ \times 0.25^\circ$	3-hourly	50S-50N	<a href="#">Huffman et al. (2007)</a>
TRMM 3B42v7	1998-2014	$0.25^\circ \times 0.25^\circ$	3-hourly	50S-50N	<a href="#">Huffman and Bolvin (2013)</a>

Table 2: List of gridded temperature datasets used in this study. All datasets consist of land surface air temperatures derived from ground-based stations across the region.

Product	Period	Spatial Resl.	Temporal Resol.	Coverage	References
APHRODITE	1951-2007	$0.25^\circ \times 0.25^\circ$	Daily	Asia	<a href="#">Yasutomi et al. (2011)</a>
CRU	1901-2013	$0.50^\circ \times 0.50^\circ$	Monthly	Global-land	<a href="#">Harris et al. (2013)</a>
UDel	1900-2012	$0.50^\circ \times 0.50^\circ$	Monthly	Global-land	<a href="#">Willmott and Robeson (1995)</a>

Table 3: Details of the three reanalyses used in this study. All datasets consist of terrestrial surface air temperatures.

Product	Period	Spatial Resl.	Temporal Resl.	Coverage	References
ERA-Interim Land	1979-2010	$0.79^\circ \times 0.79^\circ$	6-hourly	Global	<a href="#">Dee et al. (2011)</a>
MERRA Land	1980-2010	$0.67^\circ \times 0.50^\circ$	6-hourly	Global	<a href="#">Rienecker et al. (2011)</a>
CFSR	1979-present	$0.50^\circ \times 0.50^\circ$	6-hourly	Global	<a href="#">Saha et al. (2010)</a>

Table 4: Annual amplitudes of various rainfall and temperature products over the Ganges and Brahmaputra-Meghna-RBs over the period 1980-2013.

Data—	Rainfall [mm/yr]		Temperature [ $^\circ\text{C}$ ]	
	Ganges	Brahmaputra-Meghna	Ganges	Brahmaputra-Meghna
APHRODITE [1980-2007]	260.3	263.9	-	-
GPCCv6 [1980-2007]	311.7 (310.0)	351.4 (346.3)	-	-
CRU.TS3.22 [1980-2007]	284.1 (280.4)	334.5 (330.0)	6.9	7.0
TMPAv7 [1998-2013]	320.7	330	-	-
CHIRP [1998-2013]	342.4	308.8	-	-
ERA-Interim [1980-2010]	308.8	329.2	5.6	5.3
MERRA [1980-2010]	244.2	219.4	9.0	8.7
CFSR [1980-2010]	345.4	379.5	8.2	8.4

Table 5: Linear trends in rainfall (mm/decade) derived from observations and reanalysis products. Values that are significant at 95% confidence level are highlighted in bold.

Rainfall Products—	Ganges [mm/dec]				Brahmaputra-Meghna [mm/dec]			
	Winter	Spring	Summer	Autumn	Winter	Spring	Summer	Autumn
GPCCv6 [1980-2010]	-0.7	-12	0.2	<b>-2.9</b>	-0.8	0.2	-4.5	-1.9
TRMMv7 [1998-2013]	2.1	-6.1	12.4	-6.6	-0.1	-4.6	<b>-39.0</b>	-3.3
CHIRP [1998-2013]	1.1	-2.0	-7.0	-10.3	0.0	-3.9	-20.2	-9.2
ERA-Interim [1980-2010]	-1.5	-9.5	-5.8	<b>-3.6</b>	-6.8	-12.6	-6.9	<b>-2.8</b>
MERRA [1980-2010]	1.1	9.0	3.0	-2.0	5.9	<b>17.4</b>	3.0	-1.1
CFSR [1980-2010]	-0.8	18.1	1.9	-2.1	0.9	19.8	5.0	-3.2

Table 6: Linear trends in temperature ( $^{\circ}\text{C}/\text{decade}$ ) derived from observations and reanalysis products. The values that are significant at 95% confidence level are shown in bold.

	CRU_TS3.22	UDEL	ERA-Interim	MERRA	CFSR
<b>Ganges</b>					
Spring	<b>0.38</b>	<b>0.36</b>	0.08	0.16	<b>0.52</b>
Summer	0.1	0.03	-0.22	<b>-0.4</b>	-0.17
Autumn	<b>0.41</b>	<b>0.27</b>	0.08	0.21	<b>0.31</b>
Winter	<b>0.41</b>	<b>0.26</b>	0.32	<b>0.31</b>	<b>0.42</b>
<b>Brahmaputra-Meghna</b>					
Spring	<b>0.42</b>	<b>0.39</b>	0.15	<b>0.26</b>	<b>0.43</b>
Summer	<b>0.21</b>	0.09	-0.06	0.1	0.02
Autumn	<b>0.46</b>	<b>0.28</b>	0.06	<b>0.28</b>	<b>0.33</b>
Winter	<b>0.64</b>	<b>0.48</b>	0.35	<b>0.43</b>	<b>0.8</b>

Table 7: Correlation between CRU\_TS3.22 and other temperature products over the GBM RB. Correlations were computed between the PCs of first two leading modes of CRU\_TS3.22 and other products.

Temperature products	PC 1	PC 2
UDEL	0.95	0.90
ERA-Interim	0.89	0.68
MERRA	0.79	0.77
CFSR	0.41	0.48

Table 8: Correlation between SST anomalies and the first two PCs of various temperature products for the period 1981 to 2010. The correlation values that are significant at 95% confidence level are highlighted bold.

Temperature Products	Nino3.4 vs PC 2	DMI vs PC 2
CRU_TS3.22	<b>0.53</b> (at 3 month lag)	<b>0.24</b> (at 3 month lag)
UDEL	<b>0.56</b> (at 3 month lag)	<b>0.22</b> (at 3 month lag)
ERA-Interim	<b>0.35</b> (at 3 month lag)	0.05 (at 3 month lag)
MERRA	<b>0.46</b> (at 3 month lag)	0.13 (at 3 month lag)
CFSR	<b>0.27</b> (at 3 month lag)	<b>0.30</b> (at 3 month lag)

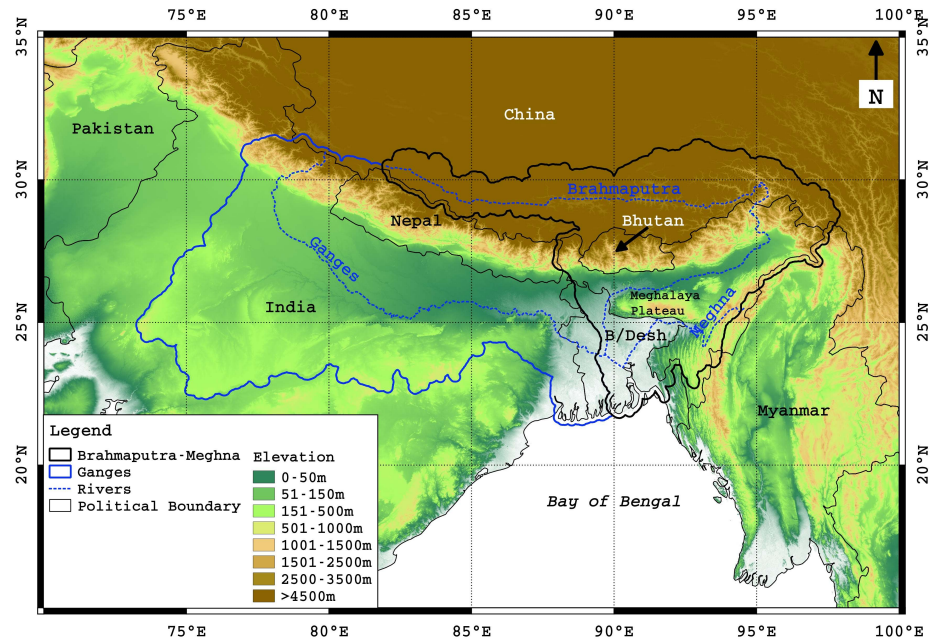


Figure 1: Overview of the Ganges-Brahmaputra-Meghna RB in South Asia. Brahmaputra and Meghna RBs are merged together, which is represented by the thick black polygon, while the Ganges River Basin is shown in thick blue polygons. This representation will be used for the remainder of this study. Source: [Khandu et al. \(2016b\)](#).

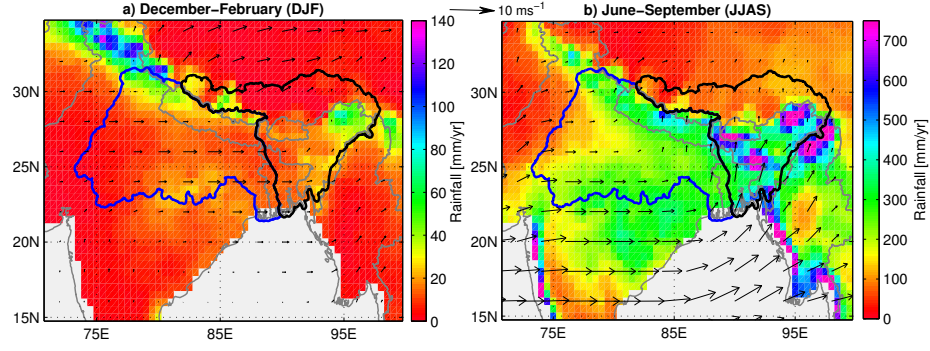


Figure 2: a) winter (DJF) and (b) monsoon (JJAS) rainfall climatology (1980–2010) based on GPCCv6 precipitation analysis over the GBM RB. The temporal mean wind fields at 850 hPa level obtained from ERA-Interim was also plotted to show the directions of winds during the two seasons.

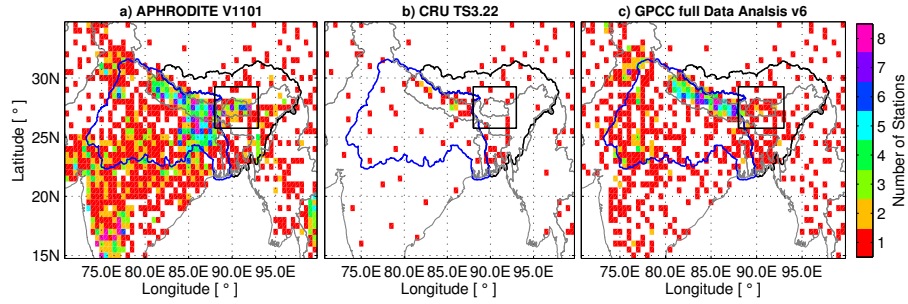


Figure 3: Spatial distribution of rain gauge stations across the GBM RB and its neighbouring regions that were used in (a) APHRODITE, (b) CRU\_TS3.22, and (c) GPCCv6. Modified from [Khandu et al. \(2016a\)](#).

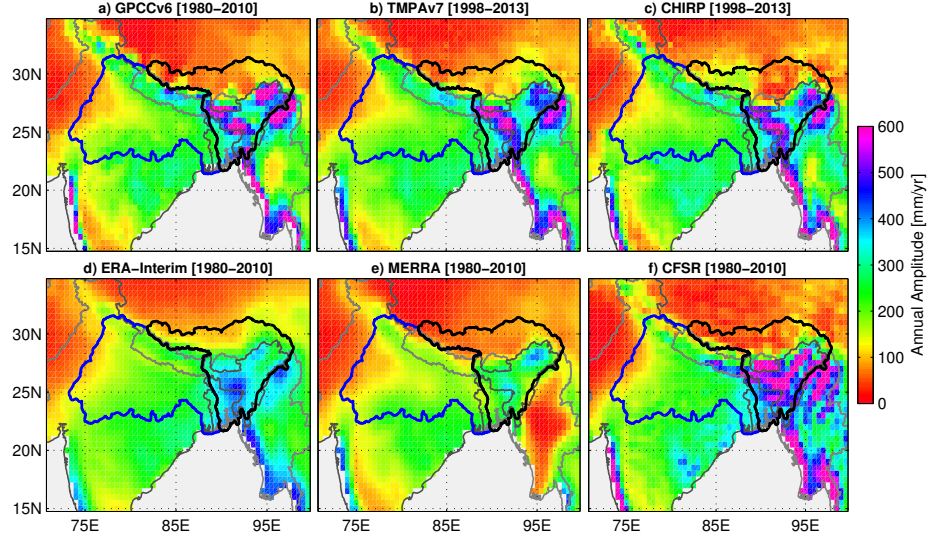


Figure 4: Spatial variations of mean annual amplitudes of monthly rainfall over the GBM RB based on a) GPCCv6 (1980–2010), (b) TMPAv7 (1998–2013), (c) CHIRP (1998–2013), d) ERA-Interim (1980–2010), e) MERRA (1980–2010), f) CFSR (1980–2010)..

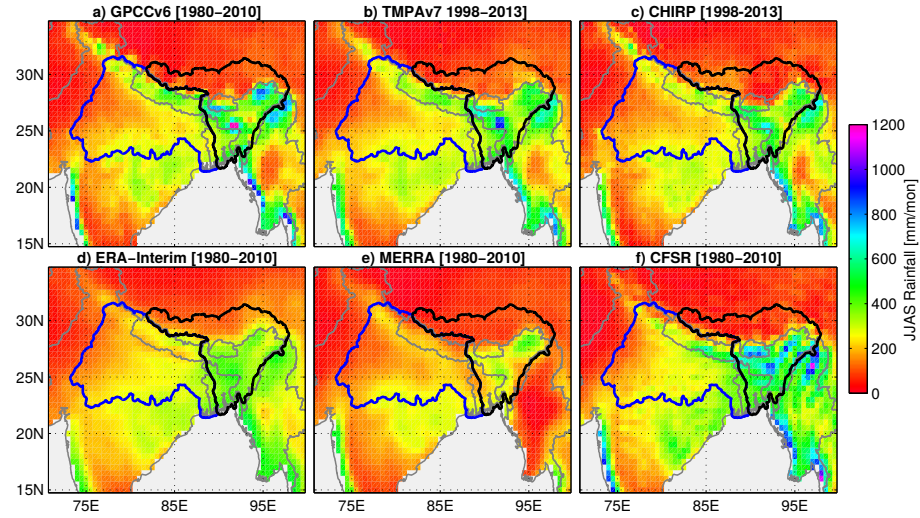


Figure 5: Spatial distribution of monsoon (JJAS) rainfall over the GBM RB a) GPCCv6 (1980–2010), (b) TMPAv7 (1998–2013), (c) CHIRP (1998–2013), d) ERA-Interim (1980–2010), e) MERRA (1980–2010), f) CFSR (1980–2010).



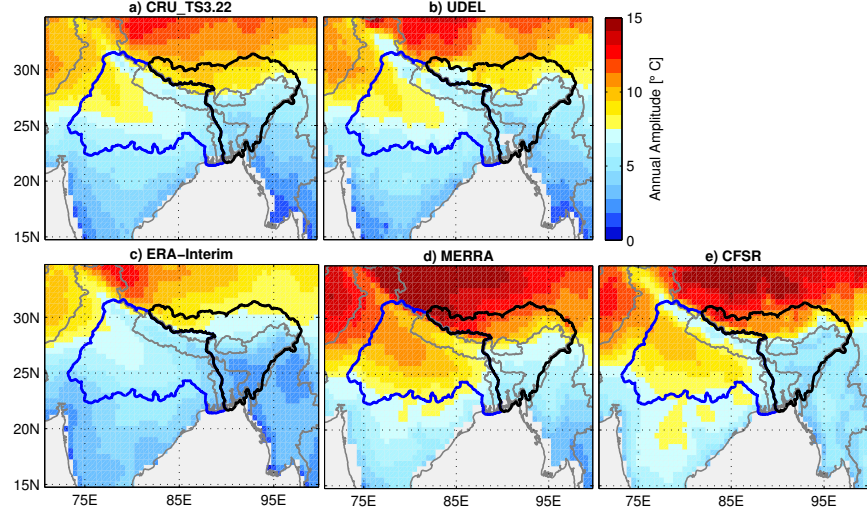


Figure 6: Spatial patterns of annual amplitudes of temperature over the GBM RB based on a) CRU\_TS3.22, b) UDEL, c) ERA-Interim, d) MERRA, and e) CFSR for the period 1980–2010.

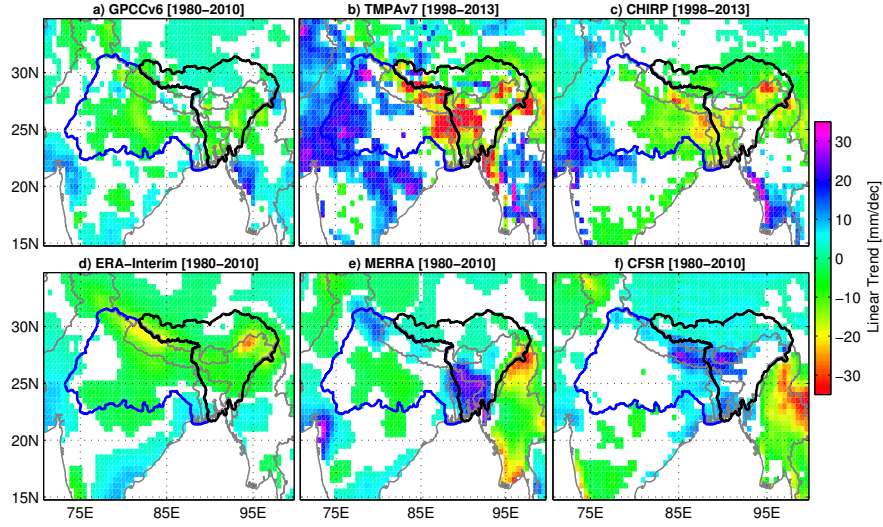


Figure 7: Precipitation changes over the GBM RB based on a) GPCCv6 (1980–2010), (b) TMPAv7 (1998–2013), (c) CHIRP (1998–2013), (d) ERA-Interim (1980–2010), (e) MERRA (1980–2010), (f) CFSR (1980–2010). Trend values that are not significant at 95% confidence level are masked out.

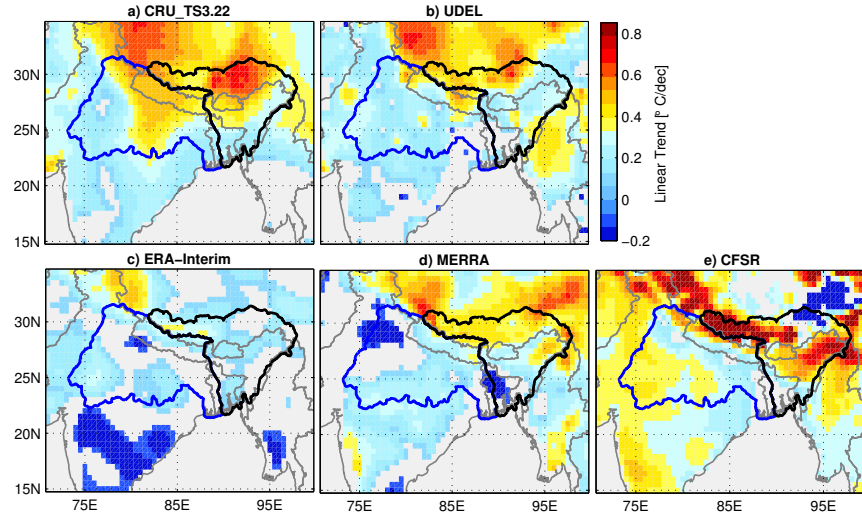


Figure 8: Spatial variation of temperature trends based on a) CRU\_TS3.22, b) UDEL, c) ERA-Interim, d) MERRA, and e) CFSR for the period 1980–2013 in the GBM RB. Trend values that are not significant at 95% confidence level are not shown.

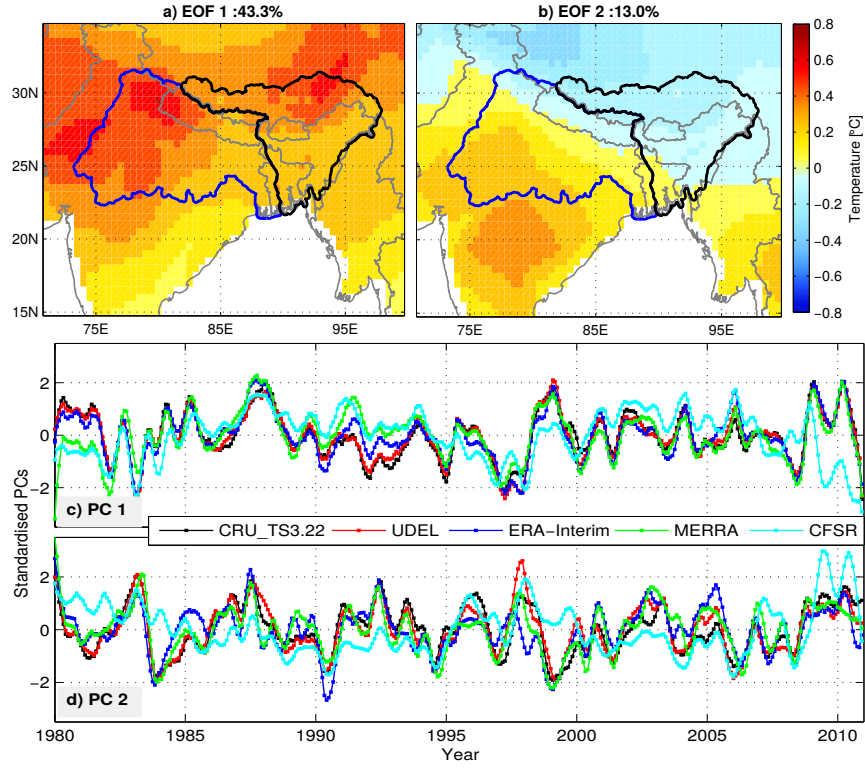


Figure 9: Spatial patterns or EOFs (a & b) and temporal components or PCs (c & d) based on first two leading modes of PCA analysis on monthly temperature anomaly of CRU\_TS3.22 over the period 1980–2013. PCs of UDEL, ERA-Interim, MERRA, and CFSR indicated in c & d are derived by projecting their respective anomalies onto the EOFs of CRU\_TS3.22.

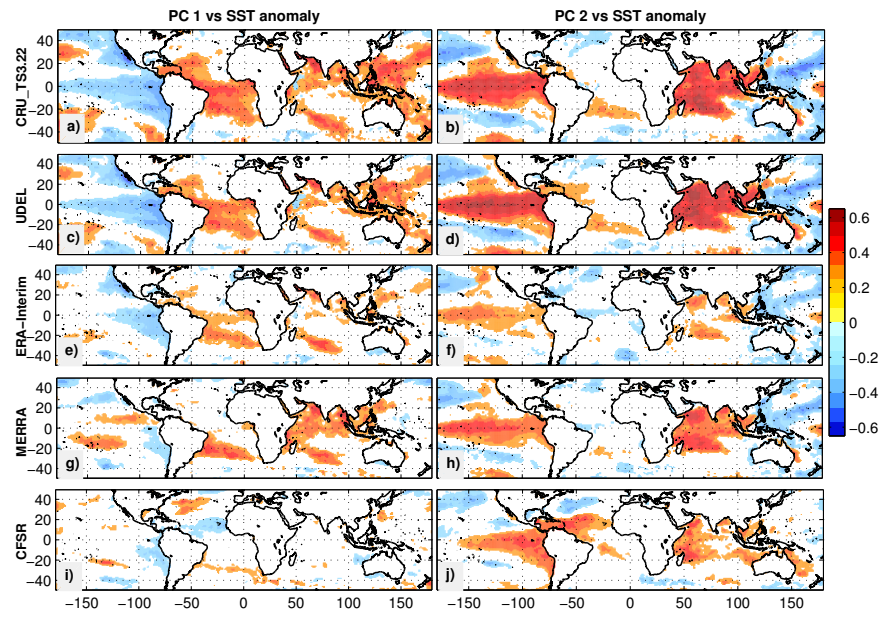


Figure 10: Correlation between the temporal components (PC 1 and PC2) and monthly SST data of HadSST over the period 1980–2013.

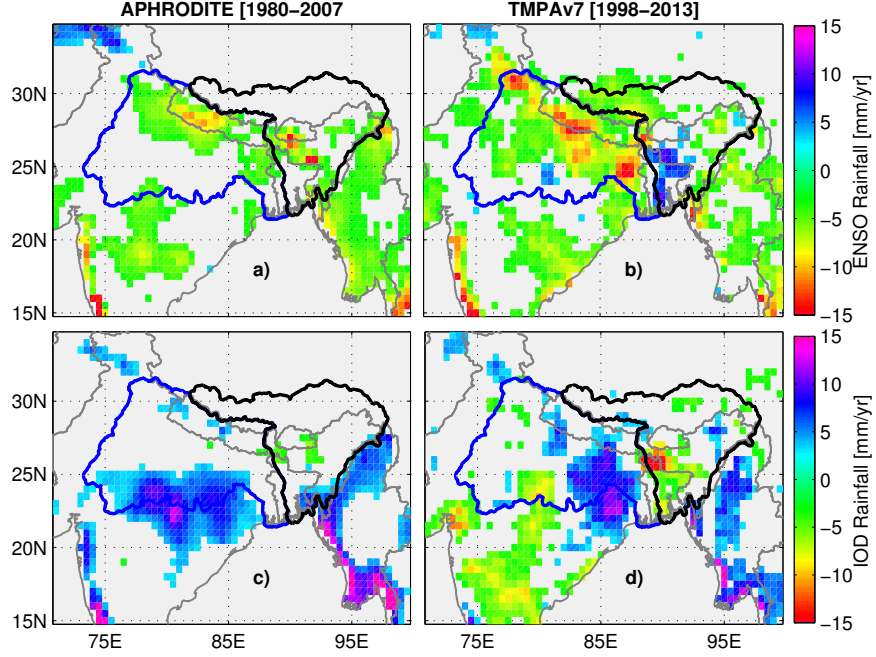


Figure 11: Regression of Niño3.4 index and DMI on precipitation anomalies of APHRODITE (1980–2007) and TMPAv7 (1998–2013). Values that are not significant at 95% confidence level based on student's  $t$ -test are not shown.

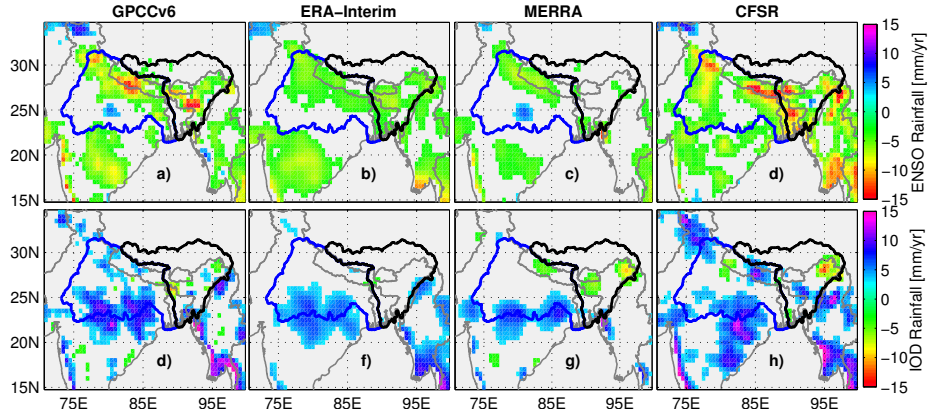


Figure 12: Regression Niño3.4 index and DMI on the precipitation anomalies of GPCCv6 and reanalysis products for the period 1980–2010. Precipitation contributions that are not significant at 95% confidence level based on student's  $t$ -test are not shown.